

Homogenized constitutive equations for porous single crystals plasticity

Cédric Sénac, J.-M. Scherer, J. Hure, T. Helfer, B. Tanguy

▶ **To cite this version:**

Cédric Sénac, J.-M. Scherer, J. Hure, T. Helfer, B. Tanguy. Homogenized constitutive equations for porous single crystals plasticity. European Journal of Mechanics - A/Solids, 2022, pp.104642. 10.1016/j.euromechsol.2022.104642 . cea-03659827

HAL Id: cea-03659827

https://cea.hal.science/cea-03659827

Submitted on 5 May 2022

HAL is a multi-disciplinary open access archive for the deposit and dissemination of scientific research documents, whether they are published or not. The documents may come from teaching and research institutions in France or abroad, or from public or private research centers.

L'archive ouverte pluridisciplinaire **HAL**, est destinée au dépôt et à la diffusion de documents scientifiques de niveau recherche, publiés ou non, émanant des établissements d'enseignement et de recherche français ou étrangers, des laboratoires publics ou privés.

Homogenized constitutive equations for porous single crystals plasticity

C. Sénac[a,*], J.-M. Scherer[a,b,**], J. Hure[a], T. Helfer[c], B. Tanguy[a]

[a] *Université Paris-Saclay, CEA, Service d'Étude des Matériaux Irradiés, 91191, Gif-sur-Yvette, France*
[b] *MINES ParisTech, PSL University, MAT – Centre des matériaux, CNRS UMR 7633, BP 87 91003 Evry, France*
[c] *CEA-Cadarache, Service d'Étude et de Simulation des Combustibles, 13108, Saint-Paul-lez-Durance, France*

Abstract

Ductile fracture through void growth to coalescence occurs at the grain scale in numerous metallic alloys encountered in engineering applications. Classical models used to perform numerical simulations of ductile fracture, like the Gurson-Tvergaard-Needleman model and its extensions, are relevant for the case of large voids compared to the grain size, in which a homogenization of the material behavior over a large number of grains is used. Such modeling prevents assessing the effects of microstructure on both crack path and propagation resistance. Therefore, homogenized constitutive equations for porous single crystals plasticity are proposed, featuring void growth and void coalescence stages, hardening and void shape evolutions. An original numerical implementation based on the coupling of Newton-Raphson and fixed point algorithms is described. In order to assess the accuracy of the proposed model as well as another one described recently in the literature, an extended database of porous unit-cell simulation results is gathered, investigating the effect of crystallographic orientations and hardening behavior for a FCC material. Strengths and weaknesses of both models are detailed with respect to the reference simulations, leading to the definition of the validity domain of the current model and to pinpoint necessary refinements.

Keywords: Ductile fracture, Porous materials, Homogenization, Single crystals, Plasticity, Constitutive equations

1. Introduction

Ductile fracture refers to a failure mode associated with a significant amount of plasticity either at the global or local scale. Various ductile fracture physical mechanisms have been observed and described experimentally depending on materials and loading conditions [1]. One of these ductile fracture mechanisms is related to the nucleation, growth and coalescence of internal voids originated from inclusions or second phase particles, widely observed in metallic alloys used in engineering applications. Ductile fracture through void growth to coalescence has been extensively studied from experimental, theoretical and numerical perspectives, and the reader is referred to the exhaustive reviews on the topic [2, 3, 4, 5]. Modeling is based on the homogenization of porous materials (Fig. 1) through different techniques [6, 7, 8], and a key ingredient is the mechanical behavior of the material surrounding voids. Classical homogenized models, such as the widely used Gurson-Tvergaard-Needleman (GTN) model [9, 10] and its anisotropic extensions [11, 12], consider von Mises or Hill associated plasticity for the matrix material. These models are relevant for polycrystalline materials where voids are significantly larger than the grain size, so that the matrix material at the scale of the voids is composed of a large number of grains (Fig. 1a) and can be described by conventional plasticity models (Fig. 1b). Interestingly, observations of fracture surfaces' dimples [5], resulting from void coalescence, and X-ray tomography experiments [13] on various metal alloys indicate that voids may be smaller than the grain size. Austenitic stainless steels (such as AISI 304 and 316) [14], aluminum alloys (AA 6xxx) [15] and Inconel alloys (IN718) [16] figure prominently among these materials. Voids size ranges typically from micrometric when nucleated from inclusions down to nanometric in specific conditions (*e.g.* nanocavities induced by irradiation [17]). In these cases, each grain is a porous single crystal (Fig. 1d).

*Corresponding author: cedric.senac@polytechnique.org
**Present address: Laboratoire Navier, École des Ponts, Université Gustave Eiffel, CNRS, Cité Descartes, 6-8 avenue Blaise Pascal, 77455 Champs-sur-Marne, France and Laboratoire de Mécanique des Solides, CNRS, École Polytechnique, Institut Polytechnique de Paris, 91128, Palaiseau, France

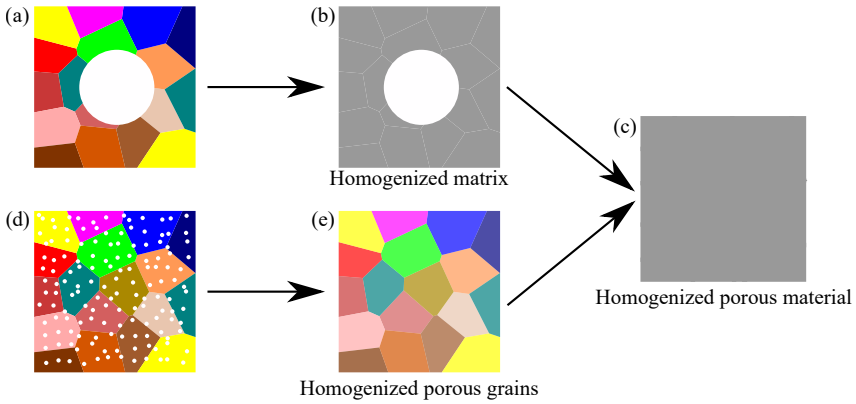


Figure 1: Homogenization strategies for porous polycrystals, for voids size larger (a) or smaller (d) than the grain size.

Any physically-based modeling of such materials thus requires to model porous single crystals. The final material behavior is then obtained either by performing a secondary homogenization over the microstructure (Fig. 1c), or by performing simulations of polycrystals (Fig. 1e). Experimental studies and theoretical modeling of porous single crystals have been tackled only recently. While detailed experimental observations of voids in single crystals under mechanical loading remain scarce, the influence of crystallographic orientation is clearly documented on both void growth mechanisms [18, 19, 20] and plasticity [21, 22]. Plasticity of porous single crystals has been assessed more extensively through porous unit-cell simulations [23, 24, 25, 26, 27] where the main results are the strong dependence of void volume fraction evolution to the crystallographic orientation, as well as a complex interplay between matrix material hardening and void growth softening as a function of stress triaxiality. Homogenized yield criteria for porous single crystals have been recently developed. Regarding void growth, several yield criteria have been proposed in the last decade based on various techniques, extending GTN-like models to single crystals. Most of them fall within the scope of multi-surface plasticity criterion [28, 29, 30, 31, 32] where each crystal slip system is kept in the homogenization procedure, while another one [33] considers a single plasticity surface. Regarding void coalescence, the well-known Thomason yield criterion model [34] has also been extended in the context of porous single crystals [25, 35, 36]. Void nucleation, mostly described classically through phenomenological laws [3], has not triggered yet dedicated models for single crystals to the authors' knowledge. All these models lead mostly to consistent and accurate predictions (with respect to reference porous unit-cell simulations) for the effect of porosity and crystallographic orientation on the yield stress of porous single crystals.

A task that is still challenging is to propose a complete set of constitutive equations for porous single crystals able to reproduce evolution problems, *i.e.*, stress-strain curves. This entails accounting for hardening, microstructural parameters evolution (porosity, crystallographic orientations, void shape) and finite strains. A first set of equations has been proposed in [37] based on the calibration and extension to finite strains of the yield criterion proposed in [28]. Comparisons of the predictions of the model to a handful of finite strain porous unit-cell simulations [37] indicate that the main features are correctly predicted, although accurate modeling of hardening is delicate. A rather complex physically-based model of porous single crystals hardening has been proposed in [27], showing promising results. Models based on the variational approach [38] have also shown predictions in good agreement with some reference simulations. For completeness, it should also be noted that other constitutive equations have been proposed for porous single crystals belonging to the damage mechanics framework [39, 40]. In both cases, a damage variable is introduced affecting the critical resolved shear stress, and its evolution is dictated either by a phenomenological law [39] or motivated by Rice & Tracey model [40]. To date, the only micromechanical-based model accounting for both void growth and void coalescence is the one proposed by [36].

The main focus of this article is bridging scales for simulating polycrystals (Fig. 1d → Fig. 1e). Indeed, numerical simulations of ductile fracture in single and poly-crystalline structures can now be achieved, as pioneered in [37] for a U-notch specimen and pursued in [36] on pre-cracked specimens. Efficient numerical implementation allows recently to perform ductile fracture simulations of a polycrystalline sample having few thousand grains [41], showing that the objective of assessing in details the effect of microstructure on fracture resistance is now within reach. Moreover, simulating ductile fracture at the polycrystalline scale opens the way to design microstructures of metal alloys – *e.g.* thanks to advanced material processing methods such as additive manufacturing – resistant to crack propagation. However, quantitative and efficient predictions require at least two ingredients. First, homogenized constitutive equations for porous single crystals should be validated and / or calibrated against an extended database of reference finite strain porous unit-cell simulations. Previous works give only few results, especially regarding the effect of crystallographic orientations that are often restricted to symmetric ones. Such database will be required to develop refined homogenized models, and is the first objective of this study. Second, constitutive equations accounting for both void growth and coalescence, as proposed in [36], may be numerically heavy due to the large number of internal variables involved. Finding a compromise between the complexity of the model and the predictive capability is definitely required, which is the second objective of this study.

The paper is organized as follows: in a first part, a database of porous unit-cell simulations results is gathered and described for a face-centered cubic material, including a large set of parameters (crystallographic orientations, hardening laws, initial void volume fractions). In a second part, a homogenized model for porous single crystals is presented, featuring both void growth and void coalescence stages, as well as simple modelling of hardening and void shape evolution. The model is different from the one proposed in [36], and is designed as simple as possible in an effort

towards industrial structure calculation scale. An original numerical implementation is proposed to increase numerical efficiency. The model proposed, as well as the alternative model [36], are assessed quantitatively to the database reference simulations. These results are then used to derive strengths and weaknesses of these complementary modelling approaches and plan future improvements of constitutive equations for porous single crystals plasticity.

2. Database for porous single crystal unit-cell simulations

In this section, crystal plasticity constitutive equations are first recalled. Then, finite strains porous single crystal unit-cell simulations are presented. All simulation results are finally gathered into a database and analyzed.

2.1. Crystal plasticity constitutive equations

Crystal plasticity constitutive equations used in the following are briefly recalled here in the context of finite strains [42]. A face-centered cubic (FCC) material is considered, but equations can be easily adapted to other crystal lattices. The deformation gradient $\underset{\sim}{\boldsymbol{F}}$ is split multiplicatively into an elastic part $\underset{\sim}{\boldsymbol{F}}_{\mathrm{e}}$ and a plastic part $\underset{\sim}{\boldsymbol{F}}_{\mathrm{p}}$:

$$\underset{\sim}{\boldsymbol{F}} = \underset{\sim}{\boldsymbol{F}}_{\mathrm{e}}\,\underset{\sim}{\boldsymbol{F}}_{\mathrm{p}} \tag{1}$$

Within the framework of crystal plasticity governed by dislocation glide, the plastic strain rate is decomposed as a sum of slip rates $\dot{\gamma}_s$ on slip systems $(\underline{n}_s, \underline{m}_s)$, where $\underline{n}_s$ denotes a slip plane normal and $\underline{m}_s$ a slip direction:

$$\dot{\underset{\sim}{\boldsymbol{F}}}_{\mathrm{p}}\underset{\sim}{\boldsymbol{F}}_{\mathrm{p}}^{-1} = \sum_{k=1}^{N} \dot{\gamma}_k\, \underline{m}_k \otimes \underline{n}_k = \sum_{k=1}^{N} \dot{\gamma}_k\, \underset{\sim}{\boldsymbol{\mu}}_k \tag{2}$$

where $\underset{\sim}{\boldsymbol{\mu}}_s$ is the Schmid tensor. Plastic slip rates are determined from a set of yield criteria S_s and rate-(in)dependent flow rules [43, 44]. Yield criteria are based on Schmid's law:

$$S_s(\tau_{\mathrm{c}}^s, \underset{\sim}{\boldsymbol{\sigma}}) = \left|\underset{\sim}{\boldsymbol{\sigma}} : \underset{\sim}{\boldsymbol{\mu}}_s\right| - \tau_{\mathrm{c}}^s = |\tau_s| - \tau_{\mathrm{c}}^s \tag{3}$$

where $\underset{\sim}{\boldsymbol{\sigma}}$ is Cauchy stress tensor, complemented with a Norton-type viscous flow rule, mainly for numerical purposes:

$$\dot{\gamma}_s = \left(\frac{S_s}{K}\right)_+^m \tag{4}$$

where $(\cdot)_+ = \max(0, \cdot)$, K and m are viscoplastic parameters that are chosen such that the results given hereafter are approximately rate-independent ($K = 10$ MPa, $m = 15$). Cubic elasticity is described by Hooke's law using Green-Lagrange strain tensor $\underset{\sim}{\boldsymbol{E}}_{GL} = \frac{1}{2}(\underset{\sim}{\boldsymbol{F}}_{\mathrm{e}}^T\underset{\sim}{\boldsymbol{F}}_{\mathrm{e}} - 1)$. Cubic symmetry elasticity moduli are given in Table 1. The critical resolved shear stress (CRSS) τ_{c}^s represents the shear stress to be applied in order to activate dislocation glide and therefore accounts for strain hardening effects. The first hardening law is the dislocation density-based model introduced in [45, 46] that will be referred to as FBZ hardening in this article. In this law, the critical resolved shear stress τ_{c}^s of a given system s is composed of a thermal component due to lattice friction τ_0 and an athermal component due to dislocations interactions:

$$\tau_{\mathrm{c}}^s = \tau_0 + \mu\sqrt{\sum_{k=1}^{N} a_{sk} r_{\mathrm{D}}^k} \tag{5}$$

where μ is the shear modulus and (a_{sk}) a matrix describing interactions between dislocations. For FCC crystals with the $\{111\}\langle 110\rangle$ slip system family, the latter is only composed of six independent coefficients a_i, with $i \in [\![1, 6]\!]$, describing the intensity of different dislocation interactions, namely: self-hardening interactions, coplanar interactions, Hirth locks, colinear interactions, glissile junctions, and Lomer locks. The shape of this matrix can for instance be found in [47]. r_{D}^k denotes the adimensional dislocation density ($r_{\mathrm{D}}^k = b^2\rho_{\mathrm{D}}^k$ where ρ_{D}^k is the usual dislocation density, *i.e.* the length of dislocation lines per unit volume, b being the norm of the dislocation Burgers vector $\underline{b}$). The evolution of dislocation densities is given by the following rate equations:

$$\dot{r}_{\mathrm{D}}^s = \left(\frac{1}{K_0}\sqrt{\sum_{k=1}^{N}(1 - \delta_s^k) r_{\mathrm{D}}^k} - G_0 r_{\mathrm{D}}^s\right)|\dot{\gamma}_s| \tag{6}$$

where δ_k^s is the Kronecker symbol which is equal to 1 if $s = k$ and 0 otherwise. Parameter K_0 is related to the pinning of dislocations while G_0 accounts for annihilation of dislocation dipoles during dynamical recovery. Numerical values used for porous single crystal unit-cell simulations are given in Table 1 and corresponds to a 304L stainless steel [28, 48], in which case $b = 0.254$ nm.

The second hardening law is the phenomenological model proposed by [49], referred to as the Peirce-Asaro-Needleman (PAN) hardening law, which links the evolution of the critical resolved shear stress τ_{c}^s of system s to the plastic slip rates $\dot{\gamma}_k$ as follows:

$$\dot{\tau}_{\mathrm{c}}^s = \sum_{k=1}^{N} d(s, k) h(\Gamma)\, |\dot{\gamma}_k| \tag{7}$$

where $\Gamma = \sum_k \int_0^t |\dot{\gamma}_k| \mathrm{d}t$ is the accumulated plastic slip. The function d represents the interaction between slip systems, while h defines the evolution of hardening as a function of Γ. These functions are given below:

$$h(\Gamma) = h_0 \cosh\left(\frac{h_0 \Gamma}{\tau_{\mathrm{sat}} - \tau_0}\right)^{-2} \tag{8}$$

$$d(s,k) = \delta + (1-\delta)\delta_k^s \tag{9}$$

τ_0 is the initial critical resolved shear stress, while h_0 is the strain hardening slope at initiation of plastic slip. $h(\Gamma)$ tends to 0 when Γ goes to infinity and leads to the saturation of τ_{c}^s towards τ_{sat}. If the parameter δ is equal to 0, the plastic slip rate on a given system s does not induce strain hardening on any other slip system ($k \neq s$) than itself, *i.e.* only self-hardening is considered, whereas for $\delta = 1$ all critical resolved shear stresses τ_{c}^s have the same evolution. Several combinations of the parameters τ_0, h_0, τ_{sat} and δ are considered in the following to model low to medium hardening. Numerical values of these parameters are presented in Table 1. Finally, as a reference, simulations are also performed without hardening, *i.e.*, $\tau_{\mathrm{c}}^s = \tau_0$.

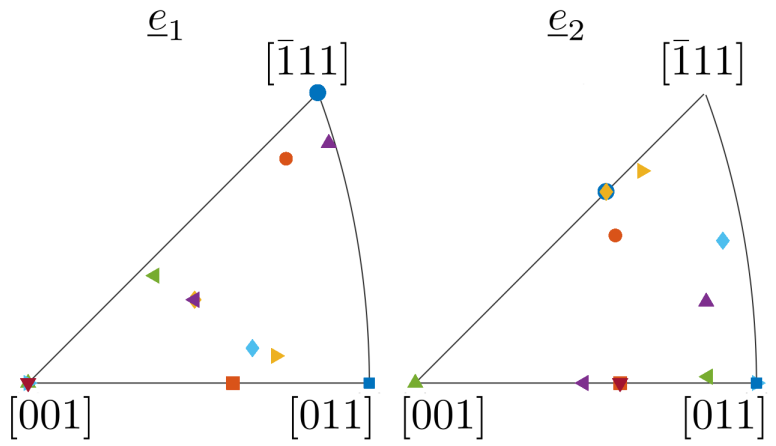
Viscosity parameters			Elasticity stiffness moduli (Mandel notation)								
	K (MPa)	m	C_{11} (GPa)		C_{12} (GPa)		C_{44} (GPa)				
	10	15	199		136		105				
Strain hardening law											
Franciosi-Berveiller-Zaoui [45, 46] – numerical values from [50]											
1a	τ_0 (MPa)	μ (GPa)	$r_{\mathrm{D}}^k(0)$	a_1	a_2	a_3	a_4	a_5	a_6	G_0	K_0
	88	65.6	$5.38 \cdot 10^{-11}$	0.124	0.124	0.07	0.625	0.137	0.122	10.4	42.8
Peirce-Asaro-Needleman [49]											
	τ_0 (MPa)		τ_{sat} (MPa)		h_0 (MPa)		δ				
2a	100		150		250		1				
2b	100		150		500		1				
2c	100		200		250		1				
2d	100		200		500		1				
2e	100		150		250		0.75				
2f	100		150		500		0.75				
2g	100		200		250		0.75				
2h	100		200		500		0.75				

Table 1: Material parameters used for porous unit-cell crystal plasticity simulations.

Numerical integration of the crystal plasticity constitutive equations detailed above has been performed according to a fully implicit scheme solved with a Newton-Raphson algorithm. Details about the implementation and finite strain framework can be found elsewhere [48].

2.2. Porous unit-cell simulations

Finite strain porous unit-cell simulations have been used extensively in order to assess the behavior of porous materials in the context of ductile fracture, and to validate homogenized models. This technique was used for porous single crystals in a relatively limited number of studies [23, 24, 25, 37, 26]. Non-linear simulations being numerically expensive, these studies usually consider few crystallographic orientations and only one set of hardening parameters. In order to construct a database on which homogenized models can be validated, 13 different FCC crystallographic orientations are considered (Fig. 2). In the Inverse pole figure (IPF) representation, the axes of the axisymetric loading ($\underline{e}_1$, $\underline{e}_2$) are given in the crystal frame. Eight symmetric orientations were chosen in order to activate simultaneously multiple slips systems. Multiple slip activation is in fact favorable for void growth. Five other orientations were picked randomly from a uniformly distributed orientation density function. These less symmetric orientations are less favorable to multiple slip system activation, but still lead to void growth due to the heterogeneous stress field around the void and because lattice rotation can turn the crystal to a more symmetric orientation favoring multiple slip.



(a)

	#	ϕ_1 (°)	Φ (°)	ϕ_2 (°)
●	0	125.3	45	180
■	1	333.4	0	0
♦	2	114.1	90	63.4
◀	3	112.1	80.2	86.1
▲	4	0	0	0
▶	5	0	45	0
▼	6	0	26.6	0
■	7	315	0	0
●	r1	124.4	34.2	267.6
▶	r2	117.8	107.4	66.8
▲	r3	141.7	101	29.1
◀	r4	16.8	55	63.5
♦	r5	142.7	53.4	29.4

(b)

Figure 2: (a) Inverse pole figure representation and (b) Euler angles (Bunge convention) of the crystallographic orientations.

Cubic unit-cells containing a centered single spherical void are considered with two different initial porosities $f \in \{0.01, 0.001\}$. Periodic boundary conditions are used along with axisymmetric loading conditions [37], principal axis $\underline{e}_1$ being aligned with the initial axis of the cell:

$$\underset{\sim}{\Sigma} = \Sigma_{11} \begin{pmatrix} 1 & 0 & 0 \\ 0 & \beta & 0 \\ 0 & 0 & \beta \end{pmatrix} \qquad T = \frac{\Sigma_{\mathrm{m}}}{\Sigma_{\mathrm{eq}}^{\mathrm{vM}}} \frac{1+2\beta}{3(1-\beta)} \tag{10}$$

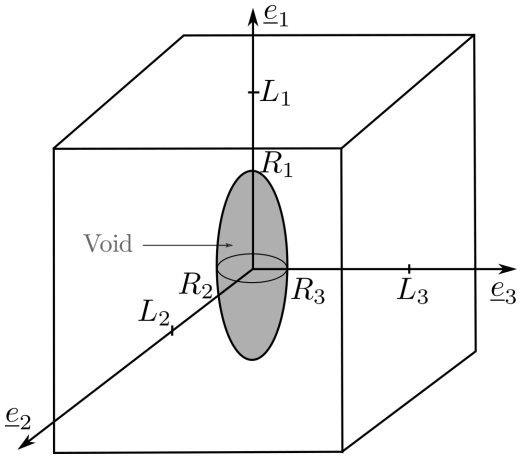
where $\Sigma_{\mathrm{m}} = \frac{1}{3}\,\mathrm{Tr}\left(\underset{\sim}{\Sigma}\right)$ is the hydrostatic stress and $\Sigma_{\mathrm{eq}}^{\mathrm{vM}}$ is the equivalent von Mises stress.

Four different values of stress triaxiality are used: $T \in \{1, 1.5, 2, 3\}$. Simulations have been performed under finite strain either in the FEM-based solver `Z-set` [51] or in the FFT-based solver `AMITEX FFTP` [52]. Mechanical loading is applied by imposing one component of the macroscopic deformation gradient rate $\dot{F}_{11} = 10^{-4}$ (FEM), $2.5 \cdot 10^{-4}$ (FFT with $T = 3$) or $7.5 \cdot 10^{-4}$ (FFT for $T = 1$), reminding that the constitutive equations used are almost rate-independent. Only cases in which $\dot{F}_{11} > 0$ are considered. Selected simulations have been performed in both solvers to check consistency of the results and discretization convergence. In the FEM-based solver, the stress triaxiality is imposed by controlling the macroscopic deformation gradient. Multiple point constraints are applied in order to impose periodic boundary conditions on homologous nodes. Details about the implementation of the boundary and loading conditions can be found elsewhere [37]. The method available in `AMITEX FFTP` is in the spirit of the work of Kabel and coworkers [53] and extended to impose proportionality on the Cauchy stress tensor.

Combining the different crystallographic orientations (Fig. 2), hardening behaviors (Tab. 1), initial porosities and stress triaxialities, 240 finite strain porous single crystal unit-cell simulations inputs and results have been gathered into a database freely accessible [54].

2.3. Analysis of the database

Under mechanical loading, the cell and the void deform from their initial shapes. Except for highly symmetric crystallographic orientations, complex shapes are obtained as strain increases, requiring the definition of simplified geometrical parameters for analyzing and comparing different simulations. Due to the boundary and loading conditions considered, cell shape remains close to orthorhombic, with the same principal axes as the initial cube and lengths L_1, L_2 and L_3 (Fig. 3). Void shape evolution is more complex, and is described as an ellipsoid of radii R_1, R_2 and R_3 (Fig. 3). This allows to define geometrical ratios of interest such as the cell aspect ratio λ (Eq. 11), void aspect ratio W (Eq. 12), intervoid normalized distance χ (Eq. 17), in addition to the porosity f (Eq. 15). The parameters λ, W and χ should be viewed as average values (according to the transverse directions) and other definitions are possible. However, in the limit of spheroidal void shape ($R_2 = R_3$) and tetragonal cell ($L_2 = L_3$) used to derive most homogenized models, classical definitions are recovered. Apart from these geometrical parameters, standard outputs of the simulations include average (over the cell volume) stress $\underset{\sim}{\boldsymbol{\Sigma}}$ and deformation gradient $\underset{\sim}{\boldsymbol{F}}$ tensors components.



$$\lambda = \frac{L_1}{\sqrt{L_2 L_3}} \quad \text{with} \quad L_1 > L_2, L_3 \tag{11}$$

$$W = \frac{R_1}{\sqrt{R_2 R_3}} \tag{12}$$

$$V_{\text{void}} = \frac{4}{3}\pi R_1 R_2 R_3 \tag{13}$$

$$V_{\text{tot}} = L_1 L_2 L_3 \tag{14}$$

$$f = \frac{V_{\text{void}}}{V_{\text{tot}}} \tag{15}$$

$$f_{\text{b}} = \frac{V_{\text{void}}}{2R_1 L_2 L_3} \tag{16}$$

$$\chi = \sqrt{f_{\text{b}}} \tag{17}$$

Figure 3: Simplified porous unit-cell geometry (left) and definition of geometrical quantities (right).

Evolution of output variables of the porous unit-cell simulations are shown in Fig. 4. Considering the entire database, a large variability is observed for the evolution of the stress Σ_{11} as a function of the deformation gradient F_{11} (Fig. 4a,b where perfect plasticity simulations are shown in insets). Accounting for such variability, coming from the interplay between the crystallographic orientation and the hardening behavior of the matrix material, is the main challenge of the development of homogenized constitutive equations for porous single crystals. Previous attempts, *e.g.*, [27, 37], have shown that this task is rather difficult. The large number of simulations in the current database allows however to gain some insights by restricting to selected subsets of entry parameters, which was not possible in previous studies that considered only few cases. Without hardening, for given stress triaxiality and initial porosity, the differences are solely due to the crystallographic orientations. For low stress triaxiality $T = 1$, as shown in Fig. 4a, a slight effect of crystallography on the apparent yield stress is observed. The effect of crystal orientation is much stronger on the value of the deformation gradient above which stress decreases abruptly (which corresponds to the onset of coalescence as discussed below). As evidenced in Fig. 4c, the increase of porosity prior to coalescence depends strongly on the crystallographic orientation. For higher stress triaxiality $T = 3$, the effect of crystallographic orientation is much weaker (Fig. 4b,d), dispersion on Fig. 4d being imputable to different hardening law parameters. Basically, higher applied stress triaxiality involves higher number of activated slip systems in the porous unit-cell. As the plastic anisotropy of FCC material is relatively weak due to the presence of 12 slip systems, a high number of activated systems involves an almost homogeneous deformation behavior whatever the crystallographic orientation. The qualitative observations made from Fig. 4 are expected to hold also for BCC materials having even more slip systems available. HCP materials are however expected to have a more complicated behavior, as described in [26], due to lower number of slip systems (with potentially different initial critical resolved shear stresses) and occurrence of mechanical twinning.

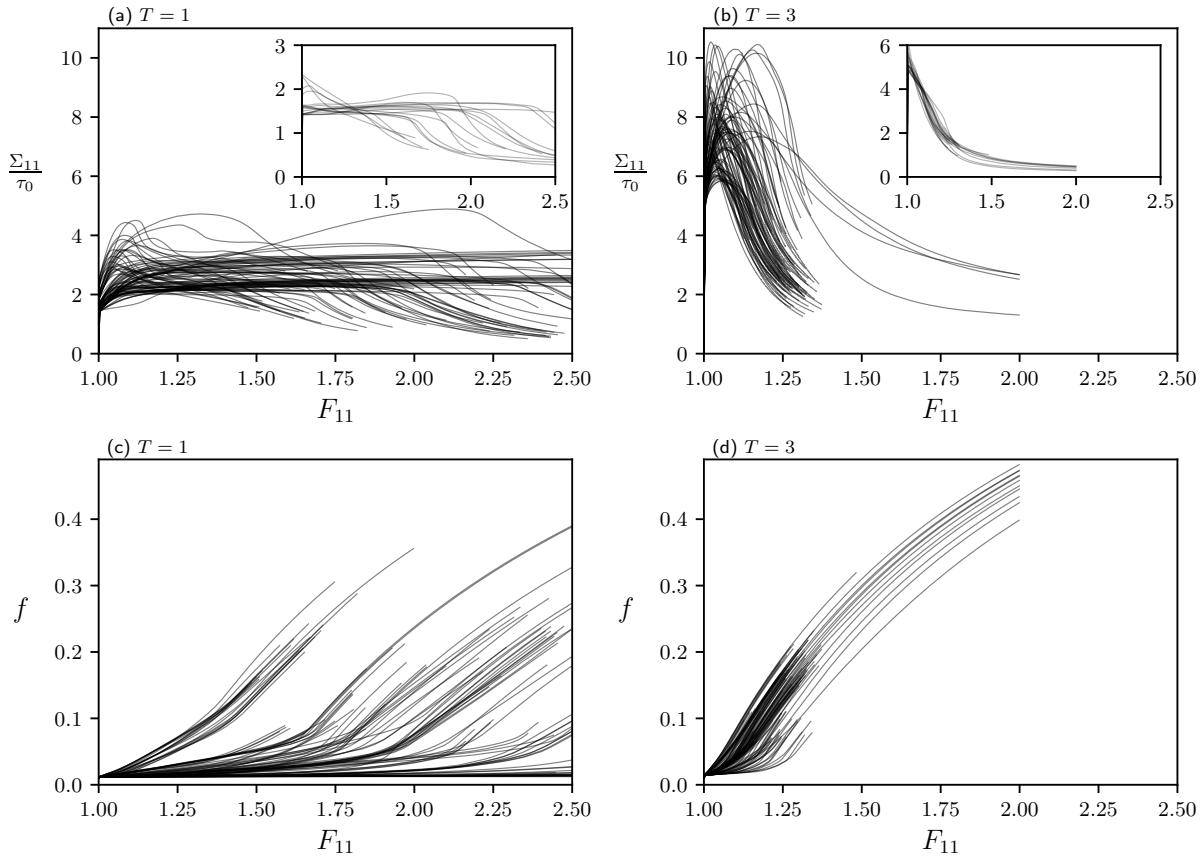


Figure 4: Evolution of the stress Σ_{11} (a,b) and porosity f (c,d) as a function of the deformation gradient F_{11}, for stress triaxiality $T = 1$ (a,c) and $T = 3$ (b,d). In (a,b), simulations with strain hardening are shown in the main plot, while simulations without hardening are shown in insets.

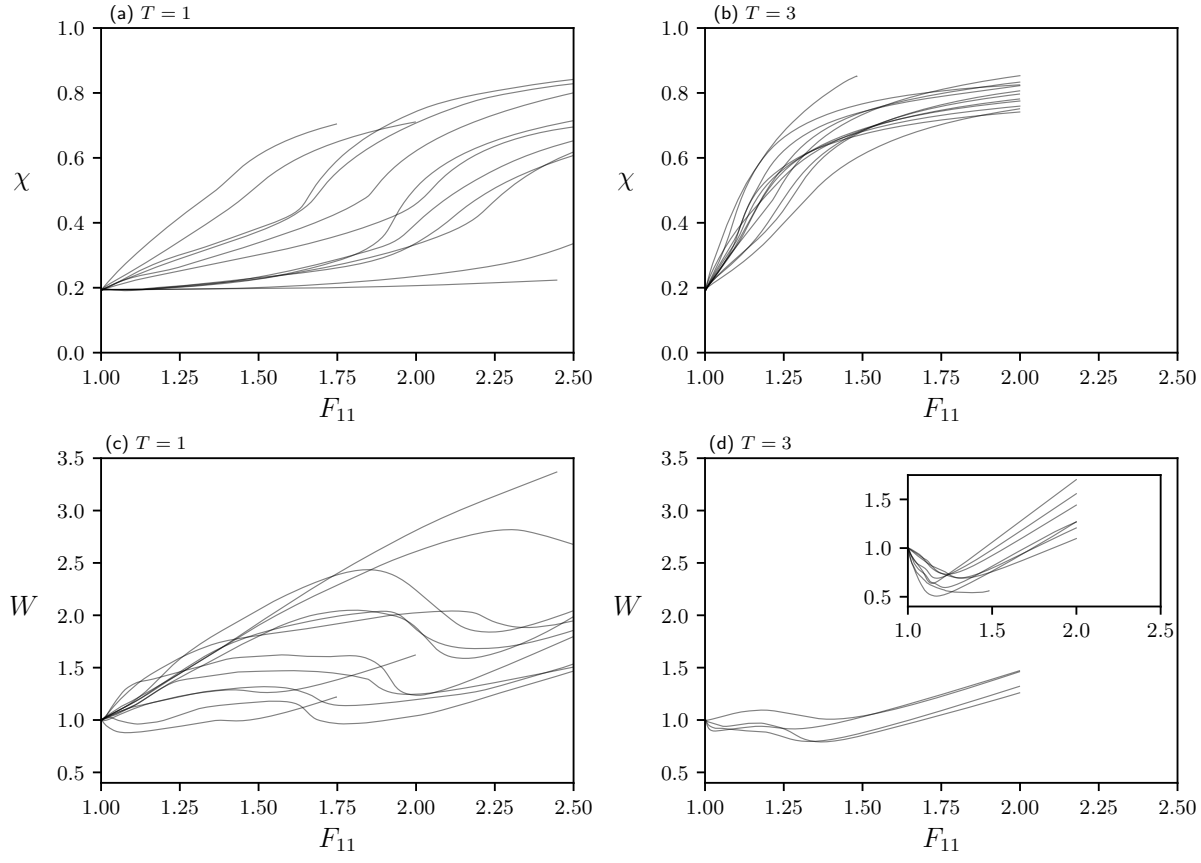
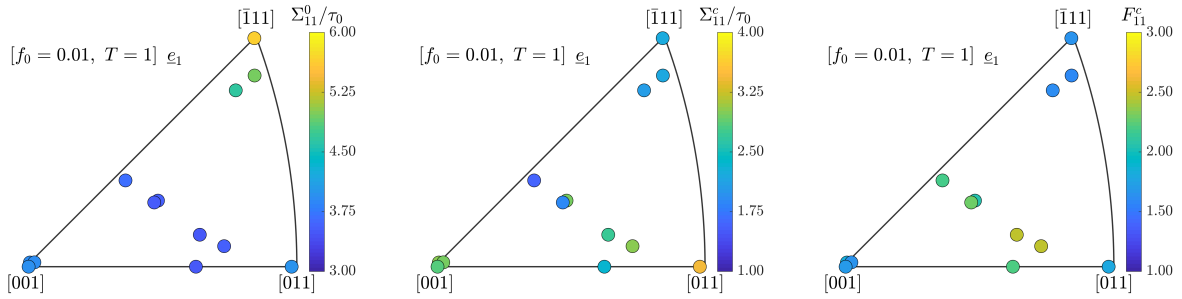


Figure 5: Evolution of intervoid normalized distance χ (a,b) and void aspect ratio W (c,d) as a function of the deformation gradient F_{11}, for stress triaxiality $T = 1$ (a,c) and $T = 3$ (b,d). Inset of (d) corresponds to cases without hardening, while the main plot displays simulation with hardening. Only FEM simulations are plotted here, contrary to Fig. 4 in which both FEM and FFT computations are shown.

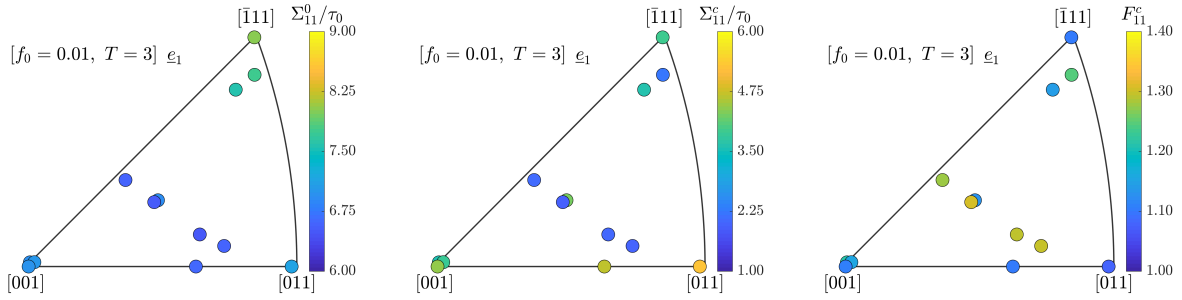
Typical evolutions of χ and W are shown in Fig. 5. In agreement with the description made on Fig. 4, more scattering is observed at low stress triaxiality ($T = 1$) compared to high stress triaxiality ($T = 3$) for both void aspect ratio and intervoid normalized distance. In average, void tends to become prolate ($W > 1$) for $T = 1$ and oblate ($W < 1$) for $T = 3$ – at least for low values of applied strain, and before void coalescence sets in. This corresponds to the typical behavior observed for isotropic porous materials [2]. However, compared to perfect plasticity cases (inset of Fig. 5d), FBZ hardening (main plot of Fig. 5d) mitigate the initial decrease of W, cavities staying almost spheroidal.

In order to gain some insights into the effects of crystallographic orientation with or without hardening, characteristic points are extracted from the curves of Fig. 4. The effective yield stress Σ^0_{11} is defined as the value of Σ_{11} for 0.2% plastic strain (similarly to conventional yield stress measured on a tensile test). The maximal stress Σ^m_{11} is also extracted, the difference with the effective yield stress allowing to quantify hardening. Finally, the onset of coalescence is defined as the occurrence of a uniaxial straining mode such as $\max\left(\dot{F}_{22}, \dot{F}_{33}\right) \leq \alpha \dot{F}_{11}$. In practice, α is set to 3%. This definition disregards the other components of the deformation gradient and thus does not account for shear-assisted coalescence mode [55]. This is justified by the initial void distribution considered – a cubic array – for which coalescence occurs mainly in the $(\underline{e}_2, \underline{e}_3)$ plane as voids are closer in that plane compared to arbitrary planes. Onset of coalescence is then defined by the corresponding values of stress Σ^c_{11} and deformation gradient F^c_{11}. Note that for some simulations – mostly at low stress triaxiality – coalescence is not attained and the corresponding values of Σ^c_{11}, F^c_{11} are not available.



(a) (b) (c)

Figure 6: Inverse pole figure representation of (a) effective yield stress Σ^0_{11}, (b) coalescence stress Σ^c_{11} and (c) coalescence deformation gradient F^c_{11} for porous single crystals with initially cubic distribution of spherical voids of porosity 1%, without hardening, for axisymmetric loading conditions with stress triaxiality $T = 1$.



(a) (b) (c)

Figure 7: Inverse pole figure representation of (a) effective yield stress Σ^0_{11}, (b) coalescence stress Σ^c_{11} and (c) coalescence deformation gradient F^c_{11} for porous single crystals with initially cubic distribution of spherical voids of porosity 1%, without hardening, for axisymmetric loading conditions with stress triaxiality $T = 3$.

The dependence of these characteristic points to the crystallographic orientations is shown in Figs. 6, 7 without hardening, and Figs. 8, 9 with hardening, using Inverse pole figure representation for the loading axis $\underline{e}_1$. For $T \in \{1, 3\}$, effective yield stress is higher for loading direction along <111>[1] (Figs. 6a, 7a), consistently with the results obtained in [27]. More interestingly, without hardening, coalescence stress (respectively deformation gradient) appears to be lower (respectively higher) in low symmetry crystallographic orientations (corresponding to the interior of the IPF) compared to high symmetry orientations (edges and corners of the IPF) especially for high stress triaxiality (Fig. 7b,c). Thus, without hardening, void growth deformation regime is active up to larger strains for low symmetry orientations. This may be explained by the fact that the increase of porosity in the void growth regime for low symmetry orientations is low, and that void coalescence depends more on the distance between voids than on the crystallographic orientations [35]. Hence, higher strains are needed to obtain the critical porosity for coalescence to happen.

[1] <111> refers to the family of equivalent FCC crystallographic directions [111], [$\bar{1}$11], [1$\bar{1}$1] etc.

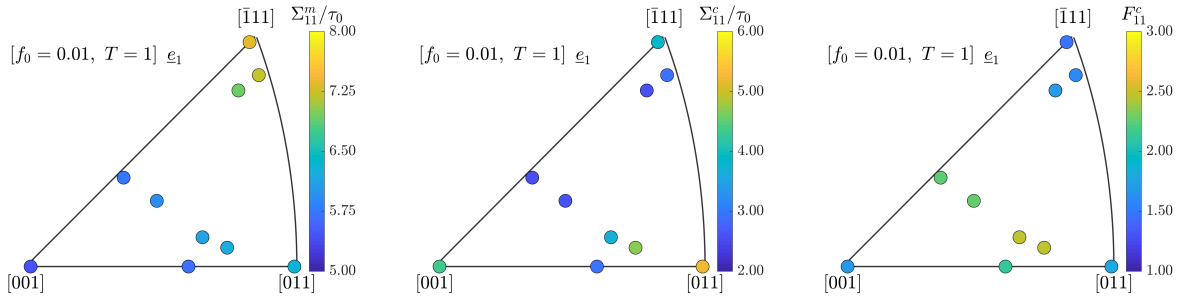


Figure 8: Inverse pole figure representation of (a) maximal stress Σ^m_{11}, (b) coalescence stress Σ^c_{11} and (c) coalescence deformation gradient F^c_{11} for porous single crystals with initially cubic distribution of spherical voids of porosity 1%, with hardening $2a$, for axisymmetric loading conditions with stress triaxiality $T = 1$.

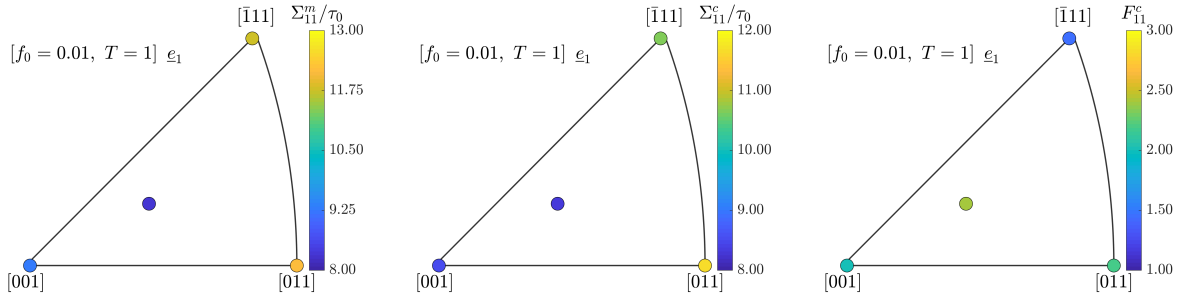


Figure 9: Inverse pole figure representation of (a) maximal stress Σ^m_{11}, (b) coalescence stress Σ^c_{11} and (c) coalescence deformation gradient F^c_{11} for porous single crystals with initially cubic distribution of spherical voids of porosity 1%, with FBZ hardening, for axisymmetric loading conditions with stress triaxiality $T = 1$.

The effect of hardening is assessed in Figs. 8, 9. For the hardening law denoted $2a$, the dependence of the maximal stress to the crystallographic orientation (Fig. 8a) is similar to the one observed for the effective yield stress (Fig. 6a). This may be understood by the fact that the hardening law defined by Eq. 7 does not depend explicitly on the orientation ($\delta = 1$ in Eq. 9): in that case, the CRSS of all slip systems remains the same during hardening. For the physically-based hardening law (denoted FBZ, see Eq. 5), differences are observed between the orientation dependence of yield stress (Fig. 6a) and maximal stress (Fig. 9a): maximal stress is for example higher for the loading direction along <011> compared to <111>, whereas the opposite is observed for the effective yield stress. The hardening rate is thus stronger along <011> compared to <111>. The interpretation of the coalescence stress values (Figs. 8b, 9b) is more difficult, notably because less crystallographic orientations were tested than in Fig. 8. However, the same conclusions than without hardening can be drawn for the coalescence deformation gradient (Figs. 8c, 9c): higher values are observed for low symmetry orientations, explained through the lower increase rate of porosity compared to high symmetry orientations. The analysis of the database of the mechanical behavior of porous FCC single crystals under axisymmetric loading conditions clearly shows the complexity associated with the interplay between porosity, crystallographic orientations and hardening. Without hardening, crystallographic orientation effect is dominant for low stress triaxiality. The effect of hardening is more difficult to interpret for physically-based hardening laws where CRSS of the different slip systems evolves differently. The challenge is thus to propose a homogenized model for porous single crystals rich enough to capture quantitatively the evolutions described in this section, but simple enough to be used in large-scale finite element simulations.

3. Homogenized model for porous single crystals

3.1. Constitutive equations

In this part, a homogenized model for porous single crystals plasticity is first presented under small strains assumption, and then extended to finite strains. $\underset{\sim}{\boldsymbol{\Sigma}}$ is the Cauchy stress tensor of the material point and is analogous to the macroscopic stress of the unit-cell. Elasticity obeys Hooke's law with cubic symmetry, $\underset{\approx}{\boldsymbol{C}}$ being the fourth-order stiffness tensor.

3.1.1. Yield criteria

Following a generic formulation proposed in [3], a yield criterion $i \in \{\mathrm{g}, \mathrm{c}\}$ ('g' stands for growth and 'c' for coalescence) will be expressed as:

$$\phi_i = \sigma_i^* - \tau^* \tag{18}$$

where τ^* is the critical resolved shear stress and σ_i^* is an equivalent scalar matrix stress implicitly defined by an equation such as $S_i(\sigma_i^*, \underset{\sim}{\boldsymbol{\Sigma}}) = 0$. The void growth regime is described by Paux-Brenner-Kondo yield criterion [33], associated with an equivalent stress σ_{g}^* defined through the following expression:

$$S_{\mathrm{g}}(\sigma_{\mathrm{g}}^*, \underset{\sim}{\boldsymbol{\Sigma}}) \equiv \left(\frac{\left(\sum_{k=1}^{N} \left| \underset{\sim}{\boldsymbol{\mu}}_k^{(\mathrm{s})} : \underset{\sim}{\boldsymbol{\Sigma}} \right|^n \right)^{\frac{1}{n}}}{\sigma_{\mathrm{g}}^*} \right)^2 + 2qf \cosh\left(\kappa \frac{\Sigma_{\mathrm{m}}}{\sigma_{\mathrm{g}}^*} \right) - 1 - (qf)^2 \tag{19}$$

In Eq. 19, κ and q are parameters that require calibration [27], $\underset{\sim}{\boldsymbol{\mu}}_k^{(\mathrm{s})}$ is the symmetric Schmid tensor of slip system k and n is a parameter used to regularize Schmid's law [56, 57] set to $n = 100$. Plastic flow is assumed to follow the normality rule, that is:

$$\underset{\sim}{\dot{\boldsymbol{\varepsilon}}}^{\mathrm{p}} \equiv \dot{p}_{\mathrm{g}} \underset{\sim}{\boldsymbol{n}}_{\mathrm{g}} = \dot{p}_{\mathrm{g}} \frac{\partial \phi_{\mathrm{g}}}{\partial \underset{\sim}{\boldsymbol{\Sigma}}} = \dot{p}_{\mathrm{g}} \frac{\partial \sigma_{\mathrm{g}}^*}{\partial \underset{\sim}{\boldsymbol{\Sigma}}} \tag{20}$$

where $\dot{p}$ is the plastic multiplier and $\underset{\sim}{\boldsymbol{n}}$ is the flow direction, indexed by g in the case of the growth criterion. For the sake of conciseness, the analytical expression of $\underset{\sim}{\boldsymbol{n}}_{\mathrm{g}}$ can be found in Appendix B.

A second yield criterion is considered to describe void coalescence by internal necking. During this phase, the yield criterion used is a variation on Thomason model proposed in [35], whose equivalent stress σ_{c}^* is defined as follows:

$$S_{\mathrm{c}}(\sigma_{\mathrm{c}}^*, \underset{\sim}{\boldsymbol{\Sigma}}) \equiv \frac{\Sigma_I}{\sigma_{\mathrm{c}}^*} - \underbrace{\left[\frac{b}{\sqrt{3}} \left(2 - \sqrt{1 + 3\chi^4} + \ln \frac{1 + \sqrt{1 + 3\chi^4}}{3\chi^2} \right) M_1 + t(W, \chi) \left(\frac{\chi^3 - 3\chi + 2}{3\sqrt{3} W \chi} \right) M_2 \right]}_{C_{\mathrm{f}}(\underset{\sim}{\boldsymbol{\Sigma}})} \tag{21}$$

where M_1 and M_2 are average Taylor factors[2], Σ_I is the largest absolute value among principal stresses and $b = 0.9$ and $t(W, \chi)$ are fitting parameters that were calibrated in [55]. The expression of t is given below:

$$t(W, \chi) = \frac{(12.9\chi - 0.84)W}{1 + (12.9\chi - 0.84)W} \tag{22}$$

Definition of M_1 and M_2 integrals can be found in [35]. Since the coalescence criterion was derived under uniaxial extension, the expression of M_1 and M_2 depend only on the normal to the coalescence plane. To avoid computing the integrals M_1 and M_2, a Fourier interpolation is used:

$$M_i \approx \sum_{m=-L}^{L} \sum_{n=-L}^{L} \hat{M}_i(m, n) \left[\cos(2m\theta) \cos(n\phi) - \sin(2m\theta) \sin(n\phi) \right] \tag{23}$$

where $\{\theta, \phi\}$ are the spherical coordinates of the normal to the coalescence plane in the crystal frame. As shown in Fig. 10a, a good agreement is obtained between the analytical values given by Eq. 23 and the numerical values, calibrating the Fourier coefficients $\hat{M}_i(m, n)$ for $L = 5$. The orientation dependence of the parameter M_1 given by Eq. 23 is shown in Fig. 10b. Numerical values of $\hat{M}_i(m, n)$ are given in the numerical implementation of the constitutive equations [58].

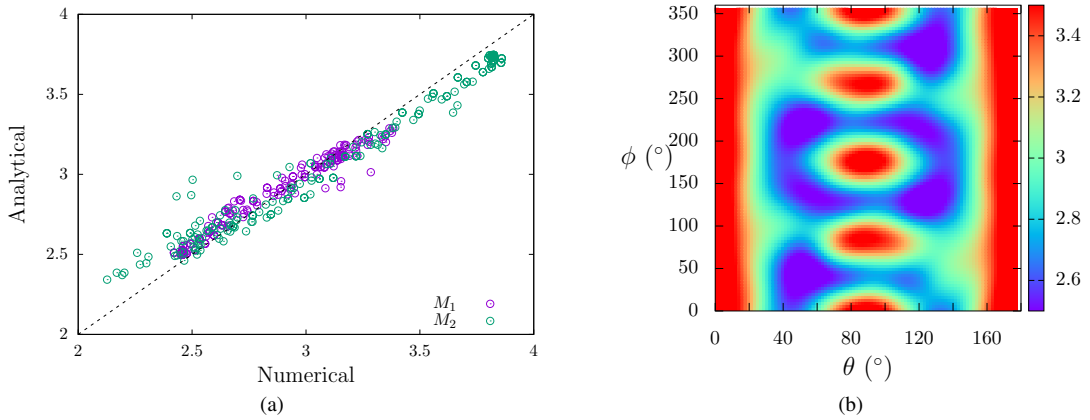


Figure 10: (a) Analytical values of the coalescence parameters M_1 and M_2 given by Eq. 23 as a function of the numerical values computed according to [35]. (b) Orientation dependence of the parameter M_1 given by Eq. 23. θ and ϕ are the spherical coordinates of the coalescence plane normal in the crystal frame.

[2]Taylor factor is defined as $M = \frac{1}{d_{\mathrm{eq}}} \sum_s \dot{\gamma}_s$ $\left(\text{with } d_{\mathrm{eq}} = \sqrt{\frac{2}{3} \dot{\epsilon} : \dot{\epsilon}} \right)$ to quantify the amount of plastic slip in a single crystal [35].

The flow rule associated with the coalescence yield criterion is:

$$\dot{\underset{\sim}{\boldsymbol{\varepsilon}}}^{\mathrm{p}} = \dot{p}_{\mathrm{c}} \frac{\partial \phi_{\mathrm{c}}}{\partial \underset{\sim}{\boldsymbol{\Sigma}}} = \dot{p}_{\mathrm{c}} \frac{1}{C_{\mathrm{f}}} \frac{\partial \Sigma_I}{\partial \underset{\sim}{\boldsymbol{\Sigma}}} \tag{24}$$

where the dependence of M_1 and M_2 to $\underset{\sim}{\boldsymbol{\Sigma}}$ is disregarded as the parameters are fixed once coalescence sets in. Eq. 24 is detailed in Appendix B and corresponds to uniaxial straining, consistently with coalescence by internal necking.

The model belongs to the multi-surface plasticity framework. In order to combine the void growth and void coalescence criteria, a viscoplastic regularization approach similar to crystal plasticity (see Section 2.1) is adopted. Plastic multipliers related to void growth and void coalescence are chosen such as:

$$\forall i \in \{\mathrm{g}, \mathrm{c}\}, \dot{p}_i = \left\langle \frac{\phi_i}{K} \right\rangle_+^m \tag{25}$$

where K and m are viscoplastic parameters and τ^* is the critical stress for both yield criteria (see Eq. 18); its evolution will be detailed in next section. These quantities are used to define the plastic strain increment:

$$\dot{\underset{\sim}{\boldsymbol{\varepsilon}}}^{\mathrm{p}} = \dot{p}_{\mathrm{g}} \underset{\sim}{\boldsymbol{n}}_{\mathrm{g}} + \dot{p}_{\mathrm{c}} \underset{\sim}{\boldsymbol{n}}_{\mathrm{c}} \tag{26}$$

with $\underset{\sim}{\boldsymbol{n}}_{\mathrm{g}}$ and $\underset{\sim}{\boldsymbol{n}}_{\mathrm{c}}$ being the flow directions of the two yield criteria defined above. At the transition from growth to coalescence, the two deformations modes are allowed to coexist in order to smooth the mechanical behavior and avoid angular points: this overlap is for numerical purposes and is not meant to describe a physical mechanism; most of the time, only one deformation mode is active – or neither of them in the elastic regime. The smoothing depends on the parameters $\{K, m\}$ used.

3.1.2. Hardening

The homogenized model should be able to handle different kind of crystal-scale hardening behaviors such as the ones described in Section 2.2. Following Gurson's approach [6], the starting point is the Hill-Mandel lemma, which states that:

$$\underset{\sim}{\boldsymbol{\Sigma}} : \dot{\underset{\sim}{\boldsymbol{\varepsilon}}} = \frac{1}{V_{\mathrm{tot}}} \int_{V_{\mathrm{tot}}} \underset{\sim}{\boldsymbol{\sigma}} : \dot{\underset{\sim}{\boldsymbol{\varepsilon}}} \, dV \tag{27}$$

expressing that macroscopic work (on the left-hand side) is equal to microscopic work (on the right hand side). The assumption that elastic strain increments are negligible in the plastic phase is made, allowing to rewrite the lemma with plastic strains instead of total strains. It is first assumed that the critical resolved shear stress τ^* is locally the same for all slip systems and depends only on the accumulated plastic slip Γ. This assumption holds exactly for the PAN hardening law with $\delta = 1$, but is an approximation in other cases considered in Section 2.2. Considering secondly an average value of the accumulated plastic slip over the matrix material in the unit-cell, denoted $\bar{\Gamma}$, Eq. 27 can be written as:

$$\underset{\sim}{\boldsymbol{\Sigma}} : \dot{\underset{\sim}{\boldsymbol{\varepsilon}}}^{\mathrm{p}} = (1 - f)\tau^* \dot{\bar{\Gamma}} \tag{28}$$

in the growth regime. Eq. 28 stands as the definition of the average accumulated plastic slip $\bar{\Gamma}$ as τ^* is assumed to depend only on $\bar{\Gamma}$. In the coalescence phase, the hypothesis that plasticity occurs only in the ligament – *i.e.* the intervoid area – leads to a slightly different expression [59]:

$$\underset{\sim}{\boldsymbol{\Sigma}} : \dot{\underset{\sim}{\boldsymbol{\varepsilon}}}^{\mathrm{p}} = \left(\frac{1}{f_{\mathrm{b}}} - 1 \right) f \tau^* \dot{\bar{\Gamma}} \tag{29}$$

where f_{b} is defined in Fig. 3. However, these two equations tend to overestimate strain hardening for low triaxialities as well as for high plastic strains. A parameter named C is thus introduced to tone it down in these cases, defined as:

$$C(\bar{\Gamma}, \underset{\sim}{\boldsymbol{\Sigma}}) = \exp\left(\beta \frac{\bar{\Gamma}}{T} \right) \tag{30}$$

with β a calibration parameter. It should be kept in mind that Eq. 30 only deals with the range of trixialities covered by the database, but can be truncated with constant functions outside of this interval. Finally, Eq. 28 and Eq. 29 become the following evolution law for $\bar{\Gamma}$:

$$\dot{\bar{\Gamma}} = \begin{cases} \dfrac{1}{C} \dfrac{\underset{\sim}{\boldsymbol{\Sigma}} : \dot{\underset{\sim}{\boldsymbol{\varepsilon}}}^{\mathrm{p}}}{(1 - f)\tau^*} & \text{(growth)} \\ \dfrac{1}{C} \dfrac{\underset{\sim}{\boldsymbol{\Sigma}} : \dot{\underset{\sim}{\boldsymbol{\varepsilon}}}^{\mathrm{p}}}{\left(\frac{1}{f_{\mathrm{b}}} - 1 \right) f \tau^*} & \text{(coalescence)} \end{cases} \tag{31}$$

The homogenized evolution of the critical resolved shear stress τ^* is then established using hardening microscopic laws, by averaging the values on all slip systems to get a unique value. In the case of PAN hardening, Eq. 7 gives:

$$\dot{\tau}^* = h_0 \frac{1 + 11\delta}{12} \cosh\left(\frac{h_0 \bar{\Gamma}}{\tau_{\mathrm{sat}} - \tau_0} \right)^{-2} \dot{\bar{\Gamma}} \tag{32}$$

The same reasoning applied to FBZ hardening, along to the fact that $\sum_k a_{sk}$ does not depend on s [3], brings the following homogenized hardening laws:

$$\dot{r_{\mathrm{D}}} = \left(\frac{1}{K_0} \sqrt{N-1} \sqrt{r_{\mathrm{D}}} - G_0 r_{\mathrm{D}} \right) \frac{\dot{\Gamma}}{12} \tag{33}$$

$$\tau^* = \tau_0 + \mu \sqrt{\sum_k a_{1k}} \sqrt{r_{\mathrm{D}}} \tag{34}$$

which can be simplified into this unique formula:

$$\dot{\tau}^* = \frac{\mu}{24} \sqrt{\sum_{k=1}^{N} a_{1k}} \left(\frac{1}{K_0} \sqrt{N-1} - G_0 \frac{\tau^* - \tau_0}{\mu \sqrt{\sum_k a_{1k}}} \right) \dot{\Gamma} \tag{35}$$

3.1.3. Evolution of microstructural variables

Homogenization theory makes use of microstructural parameters to describe the ductile material microstructure without accounting for explicit evolution of voids. The microstructural parameters of interest have been defined in Section 2.3. These parameters are treated as internal variables of the model and follow evolution laws that are detailed thereafter. Porosity f follows a classical evolution law derived from mass conservation (see [60]):

$$\dot{f} = (1-f)\mathrm{tr}\left(\underset{\sim}{\dot{\boldsymbol{\varepsilon}}}^{\mathrm{p}}\right) \tag{36}$$

The case of void aspect ratio W is more complex, its evolution being dependent on the ductile fracture stage. During coalescence, its evolution law is obtained from geometrical considerations, as explained in [60], in the case where voids are spheroidal (with a shape factor of $\gamma = \frac{1}{2}$) and the unit-cell is orthorhombic:

$$\dot{W} = \frac{9\lambda}{4\chi} \left[1 - \frac{2}{\pi} \frac{1}{\chi^2} \right] \dot{\varepsilon}^{\mathrm{p}}_{\mathrm{eq}} \tag{37}$$

where $\dot{\varepsilon}^{\mathrm{p}}_{\mathrm{eq}} = \sqrt{\frac{2}{3} \left(\underset{\approx}{\boldsymbol{M}} : \underset{\sim}{\dot{\boldsymbol{\varepsilon}}}^{\mathrm{p}} \right) : \left(\underset{\approx}{\boldsymbol{M}} : \underset{\sim}{\dot{\boldsymbol{\varepsilon}}}^{\mathrm{p}} \right)}$ and $\underset{\approx}{\boldsymbol{M}} = \underset{\approx}{\boldsymbol{I}} - \frac{1}{3} \underset{\sim}{\boldsymbol{I}} \otimes \underset{\sim}{\boldsymbol{I}}$. However, exact evolution laws for W in the growth phase are of tedious handling (see [30] for instance). Therefore, a heuristic formula depending on triaxiality is proposed:

$$\dot{W} = \begin{cases} \dfrac{1}{W} |T-2| \, \dot{\varepsilon}_I & (T < 2) \\ -W |T-2| \, \dot{\varepsilon}_I & (T \geq 2) \end{cases} \tag{38}$$

where ε_I is the largest principal strain. With this evolution law, voids become oblate for triaxialities under 2 and prolate for triaxialities above 2, which is qualitatively in agreement with unit-cell simulations presented in Section 2.3, as well as in [25] and [61]. The simple prefactor allows to recover, on average, quantitative predictions when compared to the results shown in Fig. 5c,d, as well as a saturating behavior. The normalized intervoid distance χ appearing in Eq. 21 is computed according to:

$$\chi = q_\chi \left(\frac{6}{\pi} \frac{f\lambda}{W} \right)^{\frac{1}{3}} = q_\chi \sqrt{\frac{6}{\pi} f_{\mathrm{b}}} \tag{39}$$

This formula accounts for the difference between the unit-cell geometry from which the coalescence criterion was derived (*i.e.* a cylindrical unit-cell with a cylindrical void, see [35]) and the unit-cell geometry used to homogenize the material behavior (*i.e.* a cubical unit-cell with a spheroidal void) through the factor $\frac{6}{\pi}$. q_χ is a calibration parameter close to 1 that will be discussed later.

The small strain constitutive equations presented hereabove are extended to finite strain by using the logarithmic formalism proposed in [62] where the Hencky strain tensor $\underset{\sim}{\boldsymbol{\varepsilon}} = \frac{1}{2} \log \left(\underset{\sim}{\boldsymbol{F}}^{\mathrm{T}} \underset{\sim}{\boldsymbol{F}} \right)$ is used. As detailed in Appendix A, the final model is thus restricted in principle to highly symmetric crystallographic orientations or large porosity as rotations are disregarded[4]. This limitation will be evaluated in Section 3.4 when comparing the predictions of the model to the unit-cell simulations. Finally, the unit-cell aspect ratio λ (Fig. 3) is defined as:

$$\lambda \equiv \left(\frac{(C_I)^2}{C_{II} C_{III}} \right)^{\frac{1}{4}} = \frac{e^{\varepsilon_I}}{e^{\frac{1}{2}(\varepsilon_{II} + \varepsilon_{II})}} \tag{40}$$

where $C_I > C_{II}, C_{III}$ are the eigenvalues of Cauchy-Green tensor $\underset{\sim}{\boldsymbol{C}} = \underset{\sim}{\boldsymbol{F}}^T \underset{\sim}{\boldsymbol{F}}$ and where the equality is obtained by using logarithmic strain.

Equations of both this homogenized model (referred to as the "PBKH model") and the one presented in [36] (referred to as the "HLS model") are summarized in Appendix C for comparison and convenience. For a detailed description of

[3] For all $s \in [\![1, N]\!]$, we have $\sum_k a_{sk} = a_1 + 2a_2 + 2a_3 + a_4 + 4a_5 + 2a_6$ (see [46]).

[4] This is a result of both the definition of Hencky strain and the use of symmetric Schmid tensor $\underset{\sim}{\boldsymbol{\mu}}^{(s)}_k$ in the void growth criterion (Eq. 19).

the HLS model, the reader is referred to [36]. These two models account for both void growth and coalescence and are at the state of the art of homogenized porous crystal plasticity. However, their constituents are not identical, either on the finite strain framework (multiplicative decomposition of the deformation gradient $\underset{\sim}{\boldsymbol{F}} = \underset{\sim}{\boldsymbol{F}}_{\mathrm{e}}\underset{\sim}{\boldsymbol{F}}_{\mathrm{p}}$ versus logarithmic strain formalism) or on the level of description developed for growth and coalescence. On the one hand, HLS model uses a more complex growth criterion with one yield criterion per slip system (proposed in [28] and extended in [61]) that theoretically allows a better description of cross-hardening between slip systems but is in return more computation-intensive. On the other hand, coalescence modelling is more elaborated in PBKH model since it takes into account void shape evolution while voids retain their aspect ratio in HLS model. In their current state of development, PBKH model is implemented with both PAN and FBZ hardening whereas only FBZ hardening has been considered for HLS model.

3.2. Numerical implementation

The constitutive equations detailed in Section 3.1 form a set of nonlinear differential equations which is integrated numerically for each total strain increment $\boldsymbol{\Delta\varepsilon}$. The state variables are the elastic strain tensor $\underset{\sim}{\boldsymbol{\varepsilon}}^{\mathrm{el}}$, the porosity f, the void aspect ratio W, the average cumulated plastic slip $\bar{\Gamma}$ and the homogenized critical stress τ^* – the last two being gathered in a unique hardening state variable H since their evolution is intertwined. Other parameters involved in the constitutive equations can be deduced from these state variables, such as the stress tensor $\underset{\sim}{\boldsymbol{\Sigma}}$ from Hooke's law, cell aspect ratio λ and intervoid distance χ from geometrical relations. Equivalent matrix stresses $\sigma^*_{i\in\{\mathrm{g,c}\}}$ are obtained by solving Eqs. 19 and 21. The discretized versions of the set of equations to be solved are:

$$\begin{aligned}
\mathcal{R}_{\Delta\underset{\sim}{\boldsymbol{\varepsilon}}^{\mathrm{el}}} &= \Delta\underset{\sim}{\boldsymbol{\varepsilon}}^{\mathrm{el}} + \Delta p_{\mathrm{g}}\underset{\sim}{\boldsymbol{n}}_{\mathrm{g}} + \Delta p_{\mathrm{c}}\underset{\sim}{\boldsymbol{n}}_{\mathrm{c}} - \Delta\underset{\sim}{\boldsymbol{\varepsilon}} &&= 0\\
\mathcal{R}_{\Delta f} &= \Delta f - \mathcal{F}\left(f, \underset{\sim}{\boldsymbol{n}}_i, \Delta p_i\right) &&= 0\\
\mathcal{R}_{\Delta W} &= \Delta W - \mathcal{W}\left(\underset{\sim}{\boldsymbol{\varepsilon}}^{\mathrm{el}}, f, W, \Delta p_i, \underset{\sim}{\boldsymbol{n}}_i\right) &&= 0\\
\mathcal{R}_{\Delta H} &= \begin{pmatrix}\Delta\bar{\Gamma}\\ \Delta\tau^*\end{pmatrix} - \mathcal{H}\left(\underset{\sim}{\boldsymbol{\varepsilon}}^{\mathrm{el}}, f, W, \bar{\Gamma}, \tau^*, \Delta p_i, \underset{\sim}{\boldsymbol{n}}_i\right) &&= 0
\end{aligned} \tag{41}$$

A fully implicit integration scheme for the set of Eqs. 41 would solve the equations considering that the value of each variable corresponds to the one at the end of the time step. However, such a system is notoriously difficult to solve numerically using a Newton-Raphson algorithm due to the highly non-linear nature of Eqs. 41. This may also be related to the absence of uniqueness of the incremental problem solution. Different approaches have been proposed in the literature, from a fully implicit integration scheme [63] to the explicit integration of the geometrical variables [64]. In the latter case, it can be shown that the incremental problem falls within the scope of generalized standard materials [65], where uniqueness of the solution is guaranteed.

In order to alleviate these numerical difficulties, a mixed Newton-Raphson / fixed point algorithm is proposed in this study. Eq. 41_a is solved by a Newton Raphson algorithm with respect to the increment of elastic stain tensor $\Delta\underset{\sim}{\boldsymbol{\varepsilon}}^{\mathrm{el}}$, the other state variables being constant. The Newton-Raphson algorithm requires the computation of the derivative of Eq. 41_a:

$$\frac{\partial\mathcal{R}_{\Delta\underset{\sim}{\boldsymbol{\varepsilon}}^{\mathrm{el}}}}{\partial\Delta\underset{\sim}{\boldsymbol{\varepsilon}}^{\mathrm{el}}} = \underset{\approx}{\boldsymbol{I}} + \sum_{i\in\{\mathrm{g,c}\}}\left[\Delta p_i\left(\frac{\partial\underset{\sim}{\boldsymbol{n}}_i}{\partial\underset{\sim}{\boldsymbol{\Sigma}}}\cdot\underset{\approx}{\boldsymbol{C}}\right) - \frac{m}{K_0}\left(\frac{(\sigma_i^* - \tau^*)_+}{K_0}\right)^{m-1}\Delta t\left(\underset{\sim}{\boldsymbol{n}}_i\otimes\left(\underset{\sim}{\boldsymbol{n}}_i : \underset{\approx}{\boldsymbol{C}}\right)\right)\right] \tag{42}$$

where flow directions $\underset{\sim}{\boldsymbol{n}}_{i\in\{\mathrm{g,c}\}}$ and their derivatives are detailed in Appendix B. Upon convergence of the Newton-Raphson algorithm, Eqs. $41_{b,c,d}$ are used to compute the increments of the state variables. These two steps are repeated until stationarity of these increments. This algorithm ensures a fully implicit integration scheme of the system defined by Eqs. 41. The consistent tangent operator, required for some finite element solvers, can be computed based on Eq. 42 [66]. The numerical integration has been implemented in the `MFront` code generator [67], and the different steps are summarized in Algorithm 1. As the intervoid distance χ increases close to 1, the coalescence yield surface shrinks to a point, representing material failure. In order to avoid numerical issues in the vicinity of this point, a boolean state variable `broken` is added and set to `true` when χ reaches a critical value χ_c. In that case, the numerical integration simply returns zero stresses. As mentioned above, in order to extend these constitutive equations and their numerical integration to finite strains, the logarithmic strain framework is used. The full numerical implementation is freely available [58] and can be used in a large number of finite element solvers (*e.g.* with a UMAT-compatible interface) [67].

3.3. Calibration of numerical parameters

The first use of the database described in Section 2 is the calibration of numerical parameters that were not fixed in the homogenized model definition. Thereby, computation of κ and q from the growth yield criterion can be performed as follows: for each unit-cell simulation without hardening, a fixed number of points in the growth phase is sampled. κ and q are then computed with a least-square method to ensure that $|S_{\mathrm{g}}(\tau_0, \underset{\sim}{\boldsymbol{\Sigma}}, \kappa, q)|^2$ is as close to zero as possible over the sample of points, with $\underset{\sim}{\boldsymbol{\Sigma}}$ the macroscopic stress of the unit-cell and τ_0 the critical resolved shear stress. Note that the regularization parameter $n = 100$ is chosen for the yield criterion (Eq. 19). The minimization brings $\kappa \approx 0.49$ and $q \approx 1.66$, which is close to the values provided in [27] ($\kappa = 0.49$ and $q = 2$).

A similar calibration is performed on q_χ by minimizing the sum of $|S_{\mathrm{c}}(\tau_0, \underset{\sim}{\boldsymbol{\Sigma}}, q_\chi)|^2$ at the onset of coalescence phase of all unit-cell simulations without hardening. This optimization brings $q_\chi \approx 0.822$. However, direct comparisons between homogenized model computations and unit-cell simulations underline a discrepancy depending on stress triaxiality: coalescence occurs too early for high triaxialities ($T > 2$) and too late for low triaxialities ($T < 2$). In order to achieve a

Algorithm 1 Numerical integration of constitutive equations.

Require: State variables at the beginning of the time step $\left\{\underset{\sim}{\boldsymbol{\varepsilon}}^{\mathrm{el}}_n, f_n, W_n, \bar{\Gamma}_n, \tau^*_n, \texttt{broken}\right\}$
Require: Total strain increment $\Delta\underset{\sim}{\boldsymbol{\varepsilon}}$
if `broken` **then**
  $\left\{\underset{\sim}{\boldsymbol{\varepsilon}}^{\mathrm{el}}_{n+1}, f_{n+1}, W_{n+1}, \bar{\Gamma}_{n+1}, \tau^*_{n+1}\right\} \leftarrow \left\{0, f_n, W_n, \bar{\Gamma}_n, \tau^*_n\right\}$
else
  Compute elastic trial stress $\underset{\sim}{\boldsymbol{\Sigma}}_{\mathrm{trial}} = \underset{\approx}{\boldsymbol{C}} : \left(\underset{\sim}{\boldsymbol{\varepsilon}}^{\mathrm{el}}_n + \Delta\underset{\sim}{\boldsymbol{\varepsilon}}\right)$
  if $\mathcal{Y}\left(\underset{\sim}{\boldsymbol{\Sigma}}_{\mathrm{trial}}, f_n, W_n, \bar{\Gamma}_n, \tau^*_n\right) \leq 0$ **then** ▷ Elastic evolution
    $\left\{\underset{\sim}{\boldsymbol{\varepsilon}}^{\mathrm{el}}_{n+1}, f_{n+1}, W_{n+1}, \bar{\Gamma}_{n+1}, \tau^*_{n+1}\right\} \leftarrow \left\{\underset{\sim}{\boldsymbol{\varepsilon}}^{\mathrm{el}}_n + \Delta\underset{\sim}{\boldsymbol{\varepsilon}}, f_n, W_n, \bar{\Gamma}_n, \tau^*_n\right\}$
  else ▷ Elasto-plastic evolution
    $\left\{\Delta f, \Delta W, \Delta\bar{\Gamma}, \Delta\tau^*\right\} \leftarrow \{0, 0, 0, 0\}$
    repeat ▷ Fixed-point algorithm for $\left\{\Delta f, \Delta W, \Delta\bar{\Gamma}, \Delta\tau^*\right\}$
      $\left\{f, W, \bar{\Gamma}, \tau^*\right\} \leftarrow \left\{f_n + \Delta f, W_n + \Delta W, \bar{\Gamma}_n + \Delta\bar{\Gamma}, \tau^*_n + \Delta\tau^*\right\}$
      while $\left|\mathcal{R}_{\Delta\underset{\sim}{\boldsymbol{\varepsilon}}^{\mathrm{el}}}\right| \geq \varepsilon$ **do** ▷ Newton-Raphson algorithm on $\Delta\underset{\sim}{\boldsymbol{\varepsilon}}^{\mathrm{el}}$
        $\Delta\underset{\sim}{\boldsymbol{\varepsilon}}^{\mathrm{el}} \leftarrow \Delta\underset{\sim}{\boldsymbol{\varepsilon}}^{\mathrm{el}} - \underset{\sim}{\boldsymbol{J}}^{-1}_{\Delta\underset{\sim}{\boldsymbol{\varepsilon}}^{\mathrm{el}}} \mathcal{R}_{\Delta\underset{\sim}{\boldsymbol{\varepsilon}}^{\mathrm{el}}}$
      end while
      $\left\{\Delta f, \Delta W, \Delta\bar{\Gamma}, \Delta\tau^*\right\} \leftarrow \{\mathcal{F}, \mathcal{W}, \mathcal{H}\}\left(\varepsilon^{\mathrm{el}} + \Delta\underset{\sim}{\boldsymbol{\varepsilon}}^{\mathrm{el}}, f, W, \bar{\Gamma}, \tau^*\right)$
    until $\max\left|\Delta f^{k+1} - \Delta f^k, \Delta W^{k+1} - \Delta W^k, \Delta\bar{\Gamma}^{k+1} - \Delta\bar{\Gamma}^k, (\Delta\tau^*)^{k+1} - (\Delta\tau^*)^k\right| \leq \delta$
    $\left\{\underset{\sim}{\boldsymbol{\varepsilon}}^{\mathrm{el}}_{n+1}, f_{n+1}, W_{n+1}, \bar{\Gamma}_{n+1}, \tau^*_{n+1}\right\} \leftarrow \left\{\underset{\sim}{\boldsymbol{\varepsilon}}^{\mathrm{el}}_n + \Delta\underset{\sim}{\boldsymbol{\varepsilon}}^{\mathrm{el}}, f_n + \Delta f, W_n + \Delta W, \bar{\Gamma}_n + \Delta\bar{\Gamma}, \tau^*_n + \Delta\tau^*\right\}$
    if $\chi > \chi_c$ **then**
      `broken` $\leftarrow$ `true` ▷ Material failure
    end if
  end if
end if

better agreement, the coalescence equivalence stress σ^*_{c} must be reduced for high triaxialities and *vice versa*. This can be achieved by a dependence of q_χ on T, as proposed in [68]. Using the database, we perform a linear fit of q_χ according to T, which brings[5]:

$$q_\chi(\underset{\sim}{\boldsymbol{\Sigma}}) = 0.912 - 0.039T \tag{43}$$

As with Eq. 30, the validity of this formula only holds over the range of trixialities covered by the database, *i.e* for values of T that are not too low or too high. Values of κ, q and q_χ were calibrated on unit-cell simulations without strain hardening, but will be used in the homogenized model for plasticity with hardening as well. The only parameter that is calibrated with the database of unit-cell simulations with hardening is β. Since PAN hardening saturates naturally, the value of β has almost no effect in this case. β is thus calibrated on FBZ hardening simulations only: a minimization of the sum of $|S_{\mathrm{g}}(\beta, \underset{\sim}{\boldsymbol{\Sigma}})|^2$ over the growth phase of these unit-cell calculations gives $\beta \approx 2.883$.

Numerical parameters of the HLS model were either fitted in a previous work using a handful of small strain simulations [28] (κ, q) or calibrated using the finite strain unit-cell simulation database of Section 2 (κ^{c}, q^{c}, q_χ). Numerical parameters for both models are summarized in Appendix C.

3.4. Comparison to unit-cells results

Once the numerical parameters calibrated, the agreement of the homogenized model to the unit-cell database can be assessed to make sure that it can reproduce the great diversity of results contained therein. Note that the objective is not to confront directly PBKH and HLS models but to evaluate the agreement of PBKH model with the simulation database; in case of discrepancy and when it is relevant, HLS model will be used to check the effects of alternative working hypotheses. Two assessments were conducted: the first one to qualify the yield criteria ability to predict the stress state given the internal variables and the second one to compare homogenized model predictions with the unit-cell axisymmetrical simulations. In all cases, only part of the unit-cell stress strain curves is used for the comparison, from effective yield stress (to avoid elasticity) until stress is equal to 40% of the maximal stress. Beyond that point, meshes are strongly distorted in numerical simulations, making the stress values questionable.

[5]Note that in the framework of associated plastic flow, this induces in principle an additional term in Eq. 24. However, this term can be disregarded since it is at least one order of magnitude below the main term, ensuring that coalescence plastic flow is still compatible with uniaxial straining.

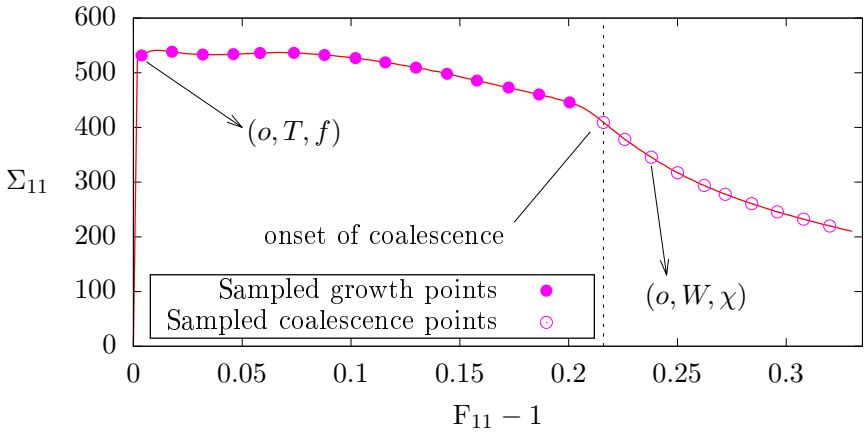
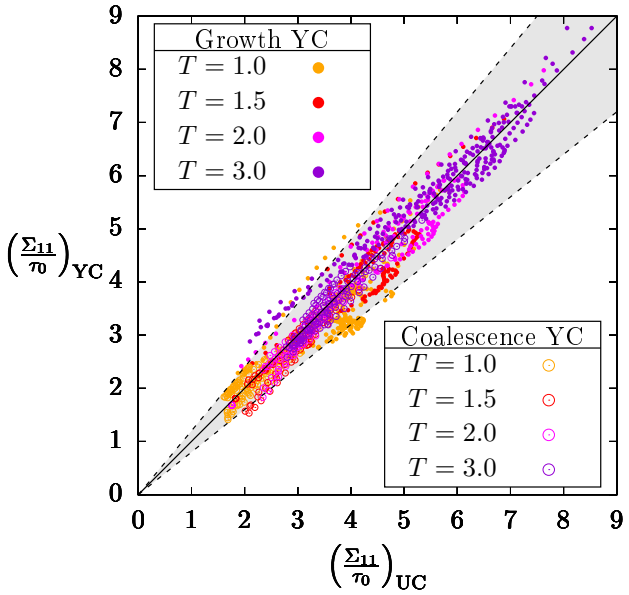


Figure 11: Outline of the sampling of points from a unit-cell simulation conducted in the first assessment: for each point, internal variables are recovered, as well as entry parameters: orientation o – for both phases – and triaxiality T – in the growth phase. The simulation represented here corresponds to $f_0 = 0.01$, $T = 2$, orientation #7 and no hardening. When a simulation is conducted with hardening, τ^* is also computed at each sampled point.

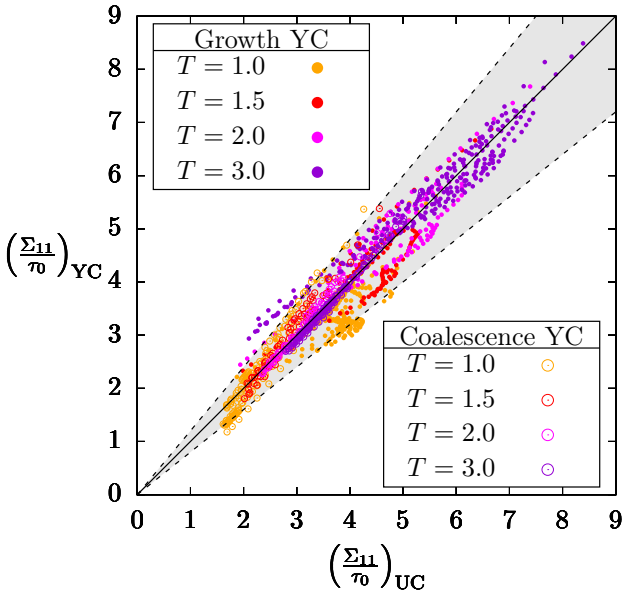
In the first assessment, points are sampled over the growth phase for each set of parameters present in the database: crystallographic orientation, triaxiality T, initial porosity f_0 and hardening law, as shown on Fig. 11. The axisymmetric stress tensor $\underset{\sim}{\boldsymbol{\Sigma}}$ is computed through equation $S_{\mathrm{g}}(\underset{\sim}{\boldsymbol{\Sigma}}, f, \tau^*) = 0$ with f and τ^* given by the unit-cell computation. $(\Sigma_{11})_{\mathrm{YC}}$ can then be compared to the unit-cell simulation stress $(\Sigma_{11})_{\mathrm{UC}}$. The same procedure is repeated by sampling points in the coalescence phase and computing $(\Sigma_{11})_{\mathrm{YC}}$ using $S_{\mathrm{c}}(\underset{\sim}{\boldsymbol{\Sigma}}, W, \chi, \tau^*) = 0$ with W, χ, τ^* given by the unit-cell simulation (see Fig. 11). Both aforementioned set of points are then displayed in Figure 12; each subgraph corresponds to a homogenized model and a hardening law[6]. For simulations without hardening τ^* is equal to the initial critical resolved shear stress τ_0, but for simulations with hardening τ^* is not directly given by the unit-cell computation, being an homogenized variable. Homogenization equations 28-35 are therefore used to compute τ^* from the unit-cell simulation stress and strain history[7]. The interest of this comparison is the assessment of the yield criteria and strain-hardening homogenization equations; this assessment is conducted independently of evolution laws, including flow rules, since geometrical internal variables are provided by unit-cell simulations. The results of this first assessment are shown in Fig. 12. Without hardening, Fig. 12a indicates that the yield criteria used in the PBKH model are very accurate *for fixed values of microstructural parameters*. This is in agreement with [27, 35] where each yield criterion has been validated. The same conclusion holds for the HLS model as shown in Fig. 12b. With hardening (Fig. 12c,d,e), more discrepancies are observed in the coalescence stage between the predictions of the homogenized models and the unit-cell results, especially in the case of FBZ hardening for which stress values are generally underestimated (Fig. 12c,d). It should be noted that the values of the parameters for FBZ hardening lead to a very strong hardening with almost no saturation unless unrealistic strain values are reached. It fosters steep hardening gradients between the bulk material that remains soft and the layer around the cavity whose hardness displays no upper bound; such heterogeneities are particularly tricky to account for with homogenized models. Restricting to low and medium hardening (PAN model), a very good agreement is obtained (Fig. 12e) between model predictions and unit-cell results whatever the parameters used (see Table 1). This shows that the extension of Gurson's modeling of hardening for crystal plasticity through Eq. 28, although simple, is effective for such situations. It should also be noted that some of the PAN hardening set of parameters correspond to cases where $\delta \neq 1$, *i.e.*, critical resolved shear stress may be locally different in each slip systems. The assumption made in the homogenized model to consider a single accumulated plastic slip $\bar{\Gamma}$ variable does not seem to degrade the results compared to cases where $\delta = 1$.

[6] In the case of the HLS model, $(\Sigma_{11})_{\mathrm{YC}}$ predicted by the growth yield criterion is the minimal value such as plasticity occurs in a given slip system $s \in [\![1, N]\!]$. The procedure applied for the coalescence criterion is the same as PBKH model with $S_{\mathrm{c}} = \frac{\Sigma_{11}}{\sigma_{\mathrm{c}}^*} - C_{\mathrm{f}}$. Relevant equations are detailed in Appendix C.

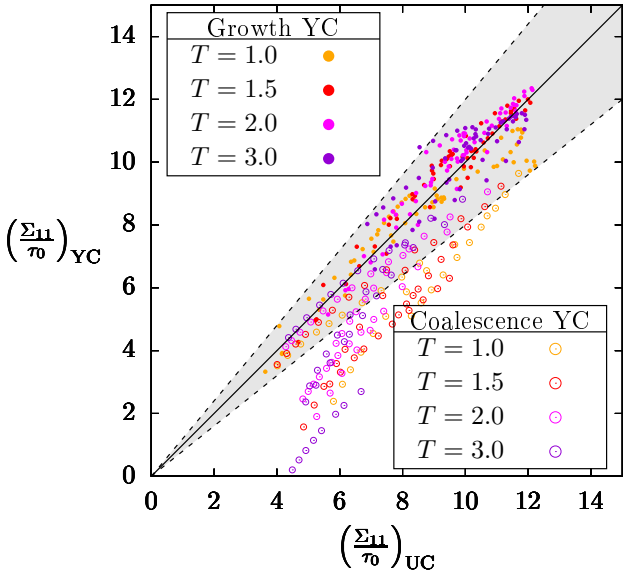
[7] Since there is no obvious way of translating this procedure for the HLS model, the same hardening homogenization equations 28-35 were applied regardless of the fact that HLS model has one homogenized critical resolved shear stress for each slip system instead of a global homogenized critical stress τ^*.



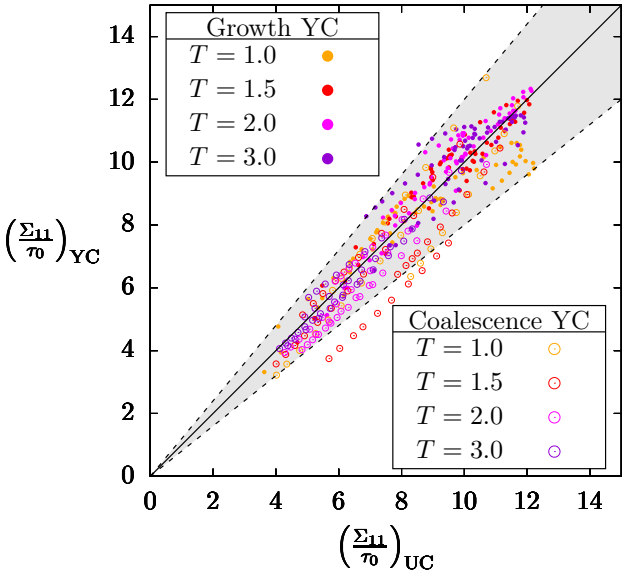
(a) PBKH yield criteria without hardening ($R_g^2 = 0.943$, $R_c^2 = 0.971$)



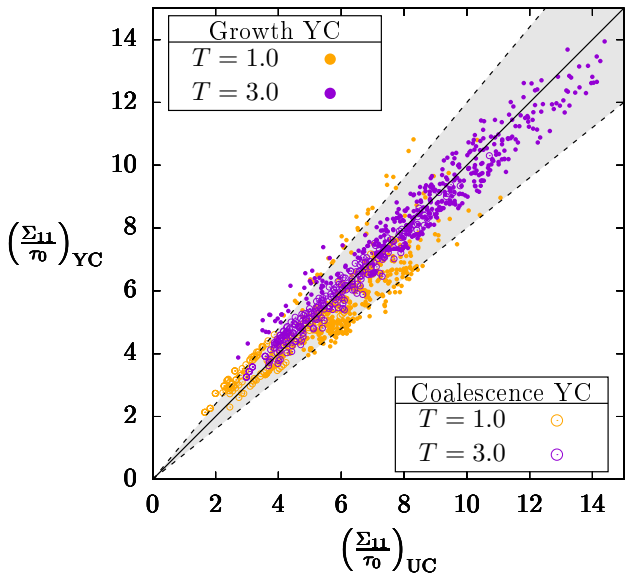
(b) HLS yield criteria without hardening ($R_g^2 = 0.937$, $R_c^2 = 0.974$)



(c) PBKH yield criteria with FBZ hardening ($R_g^2 = 0.938$, $R_c^2 = 0.836$)



(d) HLS yield criteria with FBZ hardening ($R_g^2 = 0.923$, $R_c^2 = 0.917$)



(e) PBKH yield criteria with PAN hardening ($R_g^2 = 0.948$, $R_c^2 = 0.983$)

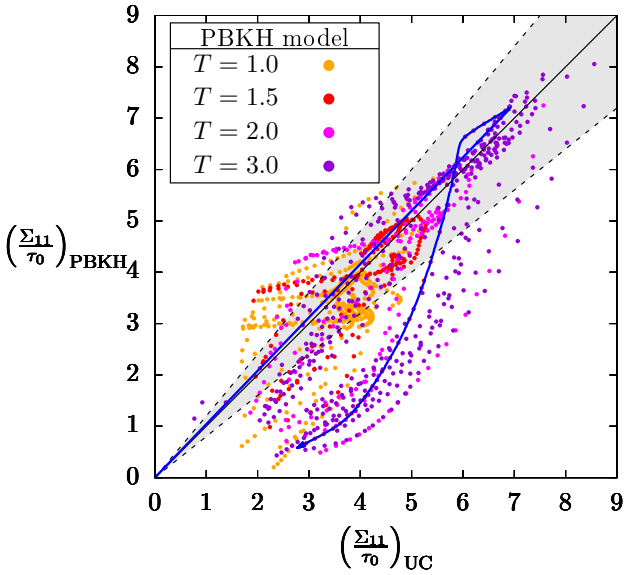
Figure 12: Assessment of yield criteria of the homogenized models: the normalized stress $\frac{\Sigma_{11}}{\tau_0}$ of the unit-cell computation and the one predicted by the yield criterion considered are plotted against each other, each point corresponding to a sampled set of internal variables from a given database simulation. Pearson correlation coefficients are given for both the growth phase and the coalescence phase of each graph. Dashed lines correspond to vertical deviations of ±20% from the $y = x$ line.

The second assessment is more straightforward: for each set of parameters present in the database, a comparison of stress values is conducted between the unit-cell computation and the predictions of both homogenized models *for fixed strain values*. Strain values are sampled for each set of parameters, *e.g.* crystallographic orientation #0 under triaxiality $T = 1.5$ without hardening. Each of those strain values corresponds to a point in Figure 13, the x-coordinate being the unit-cell normalized stress Σ_{11}/τ_0 at that strain value and the y-coordinate being the homogenized model normalized stress Σ_{11}/τ_0 at the same strain value. Contrary to Figure 12, no distinction is made between growth and coalescence as the homogenized models should be able to predict the active deformation mode, and more importantly the level of stress. This comparison allows to assess the predictive capability of the homogenized models as a whole, including yield criteria, modeling of hardening and evolution laws describing plastic flow and microstructural parameters. As yield criteria, and to a lesser extent hardening, have been shown to be rather accurate in Fig. 12, Fig. 13 stands as a test for evolution laws used in the homogenized models. For each subgraph of Figure 13, a single set of parameters is chosen and corresponding points are linked by a colored arrow in ascending strain order. The stress-strain curves of these distinctive simulations are plotted in Figure 14d,e,f.

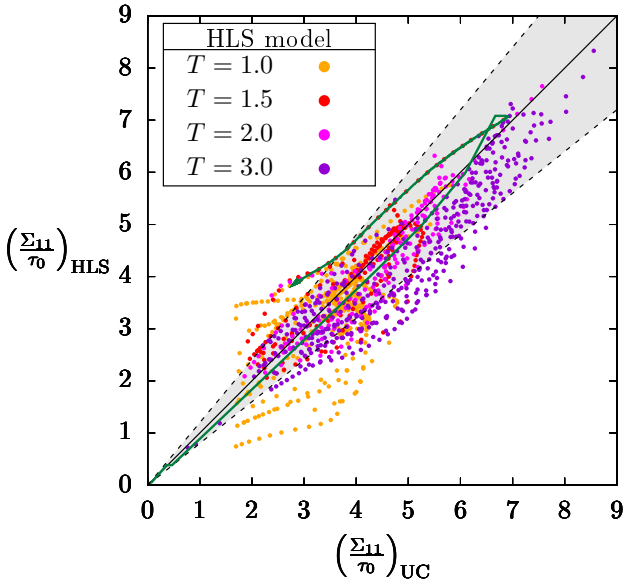
Without hardening, Fig. 13a indicates that most of the predictions of the PBKH homogenized model falls within ±20% of the unit-cell results. However, strong discrepancies are observed in certain cases where the model underestimates the stress levels. They can easily be understood by looking at the stress-strain curves (Figure 14a,b,c,d): while the model correctly predicts the first part of these curves – corresponding to void growth regime – the onset of coalescence is not predicted accurately enough, triggering a sudden stress drop that is either too late or too early. As coalescence deformation mode induces a very strong decrease of stress, the differences between the unit-cell results and the homogenized model increase drastically, explaining the strong deviations observed in Fig. 13a. In general, the representation used in Fig. 13 tends to amplify the differences, which should be kept in mind in the analysis. The HLS homogenized model appears to be in good agreement with the unit-cell results (Fig. 13a). The different behavior exhibited by the PBKH model is believed to come from at least two features. First, since the logarithmic strain framework used in the PBKH model cannot reproduce crystal lattice rotation (see Appendix A), the structural hardening coming from the progressive activation of slip systems with increasing yield limits cannot be predicted, as can be seen in Fig. 14c. A qualitative agreement is obtained for HLS model in such situations, which uses the multiplicative decomposition of the deformation gradient. This structural hardening effect, which can be strong at low triaxialities, is almost negligible at high triaxialities. Second, orientations displaying only one activated slip system under mechanical loading are not accurately predicted by PBKH model, as shown in Fig. 14d. This was expected, as discussed in the model definition, due to the use of Hencky strain tensor and symmetric Schmid tensor. In fact, orientation #0 explains the main discrepancies seen in Fig. 13a – the colored arrows on Fig. 13a,b correspond to the simulation shown in Fig. 14d – while random orientations are well predicted.

With hardening (Fig. 13c,d,e), the agreement between homogenized model predictions and unit-cell results deteriorates. For the PBKH model with FBZ hardening (Fig. 13c), the initial hardening regime is captured, but the model predicts systematically an early coalescence. For its part, the HLS model (Fig. 13d) predicts coalescence either too late or too early depending on situations, the latter being less frequent. This should not be surprising; indeed, the latter neglects the void aspect ratio evolution and thus has a simplified modeling of coalescence. The simulations marked by colored arrows in Figs. 13c,d are displayed in Fig. 14e, showing that the case of strong hardening is still difficult to handle, even though the phenomenological modification used (Eq. 30) helps to recover a prediction in closer agreement with unit-cell results. On the overall, predictions made by PBKH model with FBZ hardening display a qualitative agreement in the absence of quantitative agreement during the coalescence phase. Restricting to low to medium hardening (Fig. 13e), the agreement improves: most of the predictions falls within ±20% of the reference results, even in the coalescence regime. The simulation marked by a colored arrow is shown in Fig. 14f where a very good agreement is observed in this particular case.

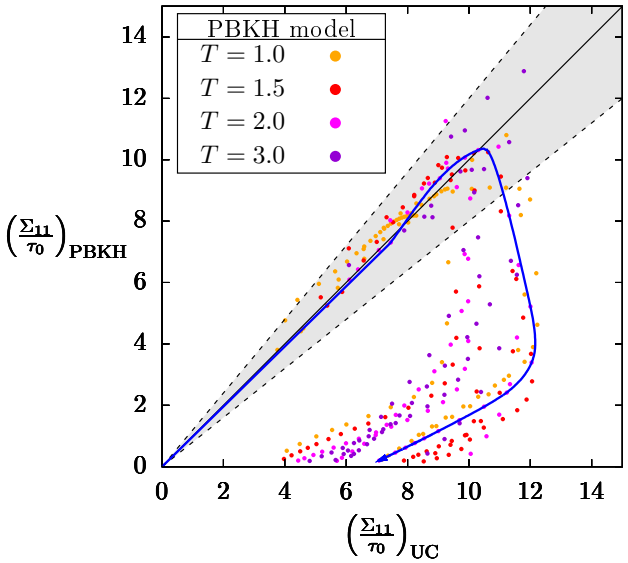
The detailed assessments conducted in this section allow drawing some conclusions regarding the current state of modeling of porous single crystals. Firstly, the model proposed in this study (PBKH), designed with a limited number of internal variables and simplified finite strain framework, leads to predictions which are for the most part in agreement with unit-cell simulations and compare quite well with the level of compliance reached by the HLS model. This implies that ductile fracture simulations can be performed using this model instead of isotropic models, *e.g.* [2], with limited additional numerical costs while accounting for the microstructure of the material. Secondly, yield criteria, and to a lesser extent hardening, are shown to be quite accurate *for fixed values of internal variables* to give quantitative stress levels under axisymmetric conditions, as shown in Fig. 12. This indicates that more efforts should be put on other factors such as the interplay between void shape changes and hardening, for example by using models derived from different approaches [30], but also on more complex – non axisymmetric – loading conditions. Finally, the proposed model displays a validity domain in which accurate predictions can be made; this will be discussed in the following section.



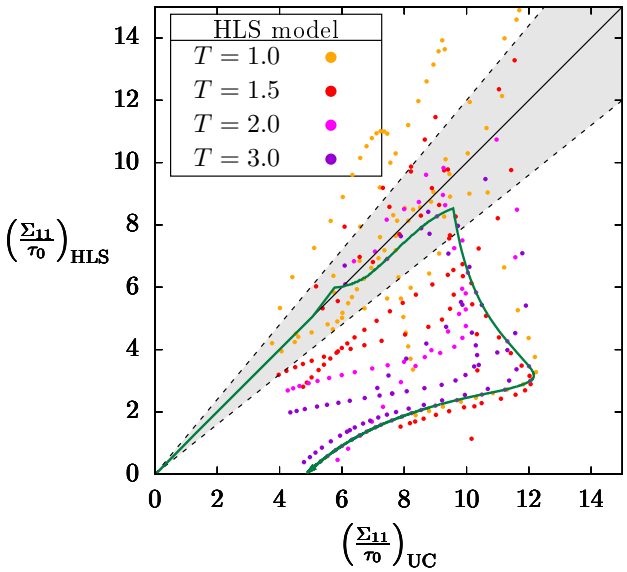
(a) PBKH model without hardening ($R^2 = 0.750$)



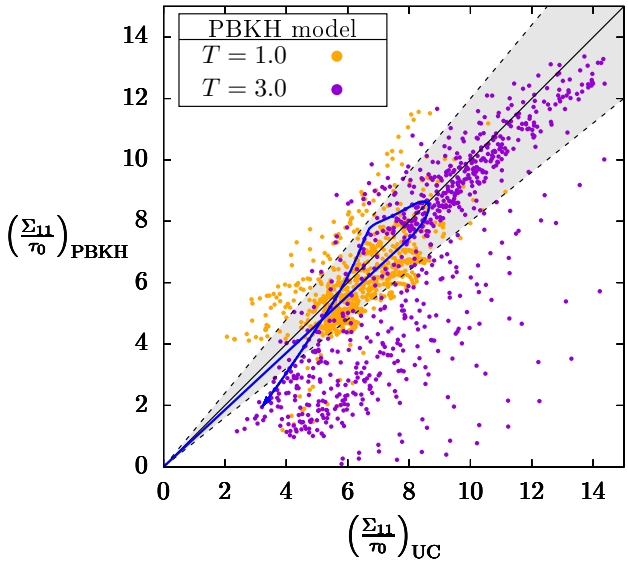
(b) HLS model without hardening ($R^2 = 0.859$)



(c) PBKH model with FBZ hardening ($R^2 = 0.318$)

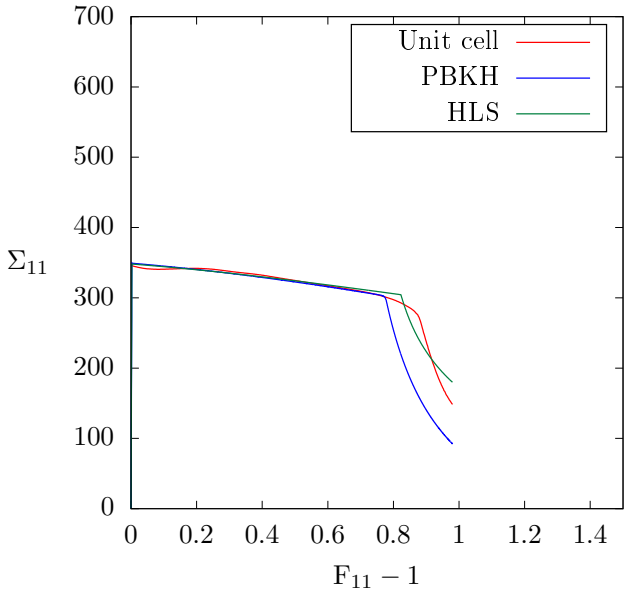


(d) HLS model with FBZ hardening ($R^2 = 0.255$)

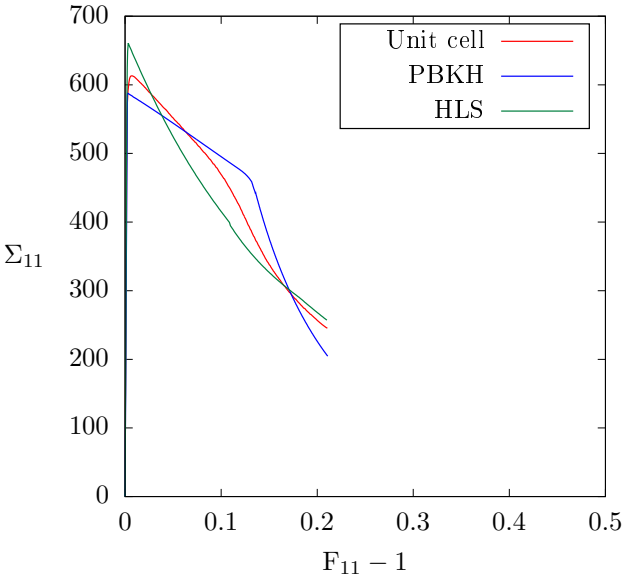


(e) PBKH model with PAN hardening ($R^2 = 0.752$)

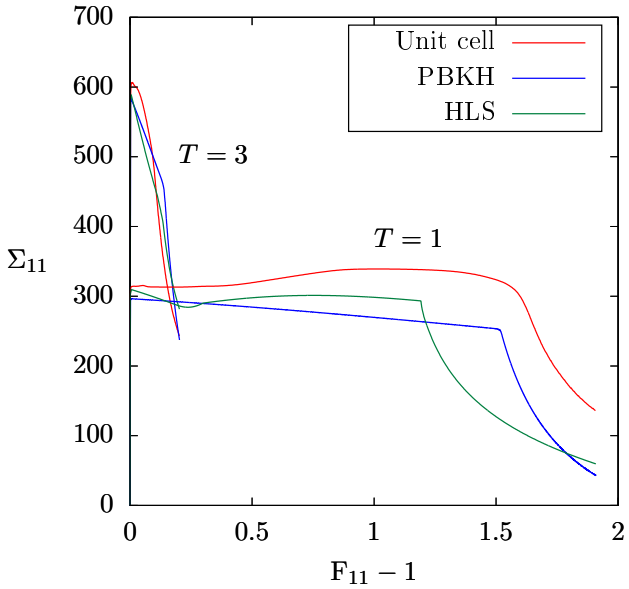
Figure 13: Assessment of the homogenized models: normalized stress $\frac{\Sigma_{11}}{\tau_0}$ of both the unit-cell computation and the homogenized model considered are plotted against each other, each point corresponding to a sampled strain level in a given database simulation. Colored arrows stand for trajectories of simulations whose stress-strain curves are plotted in Fig. 14. Pearson correlation coefficients are given for each graph. Dashed lines correspond to vertical deviations of ±20% from the $y = x$ line.



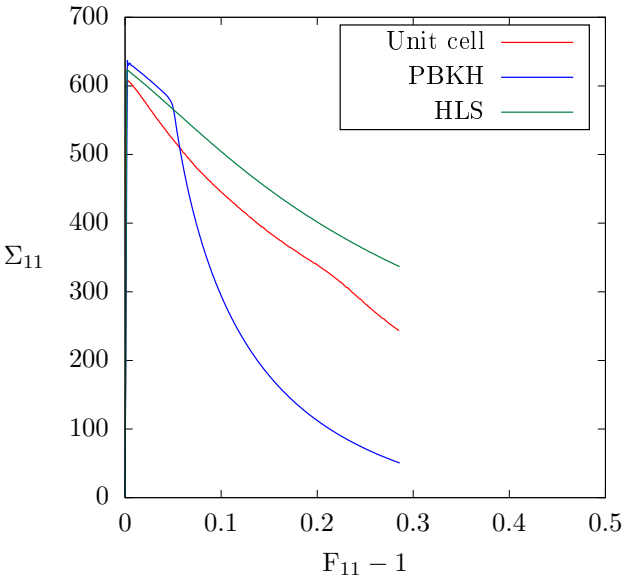
(a) Orientation #5: [1 0 0] – [0 1 $\bar{1}$] – [0 1 1], $T = 1$, without hardening



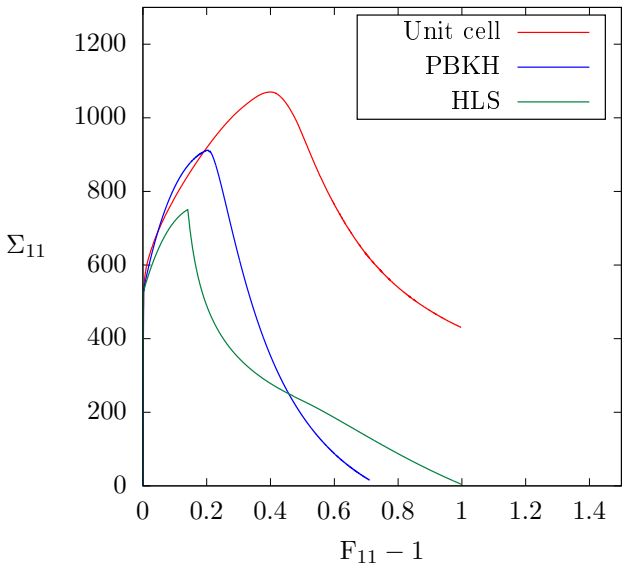
(b) Orientation #3: [$\bar{1}$ 2 5] – [0 $\bar{5}$ 2] – [29 2 5], $T = 3$, without hardening



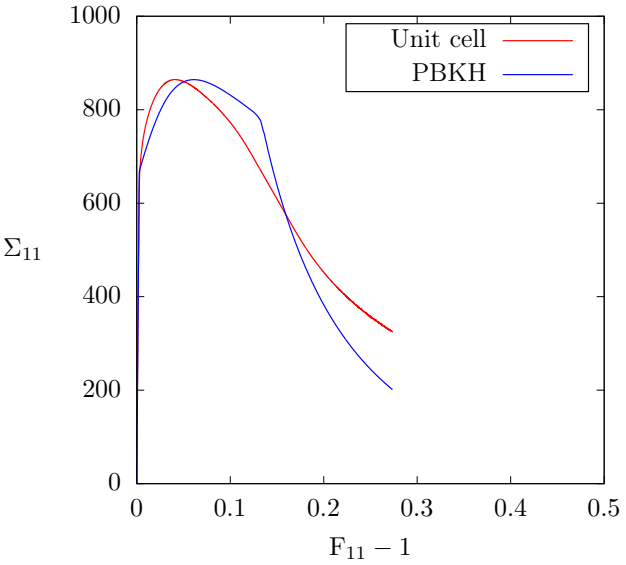
(c) Orientation #1: [2 1 0] – [$\bar{1}$ 2 0] – [0 1 1], $T \in \{1, 3\}$, without hardening



(d) Orientation #0: [1 1 1] – [$\bar{2}$ 1 1] – [0 $\bar{1}$ 1], $T = 1.5$, without hardening



(e) Orientation #7: [1 1 0] – [$\bar{1}$ 1 0] – [0 0 1], $T = 2$, FBZ hardening



(f) Orientation #2: [$\bar{1}$ 2 5] – [1 $\bar{2}$ 1] – [2 1 0], $T = 3$, PAN hardening (2b)

Figure 14: Stress-strain curves of a representative set of simulations: various orientations, triaxialities and hardening laws are considered. Comparisons are made between results of the unit-cell computation and predictions of the two homogenized models (PBKH and HLS).

4. Discussion and Perspectives

The comparisons made in the previous section call for the assessment of the domain of validity of the model proposed in this study. First, as shown in Appendix A, the finite strain framework cannot capture single slip and / or crystal lattice rotation, which is at the origin of the discrepancies observed in Figs. 14c,d. Thus, the model should be used for rather large values of the porosity or mean stress, which have been considered in this study. This is the case in highly irradiated materials where a high void volume fraction – up to tens of percent – is formed at the grain scale [17]. Another potential application is the case of materials from additive manufacturing [69]. Note that this limitation could be removed by considering the multiplicative decomposition of the deformation gradient. Secondly, strong local hardening, like the one resulting from FBZ equations (Eq. 5), cannot be captured quantitatively for all situations, even by introducing additional phenomenological modifications (Eq. 30). Considering the similar behavior displayed by the HLS model, deviations observed for the proposed model are not related to the simplifications made to account for hardening with a single hardening variable (Eq. 28). Instead, for strong hardening, a hard shell appears around the void, and local strain field is highly heterogeneous. Models have been proposed to handle this phenomenon for isotropic materials [70] that would benefit to be extended to single crystals. Considering only low and medium hardening – such as the PAN law with the set of parameters named *2a* and *2b* in Table 1 – as well as perfect plasticity cases, comparisons between unit-cell results and model predictions are shown in Fig. 15. An overall very good agreement is observed, confirming the validity of the model for low to medium hardening material.

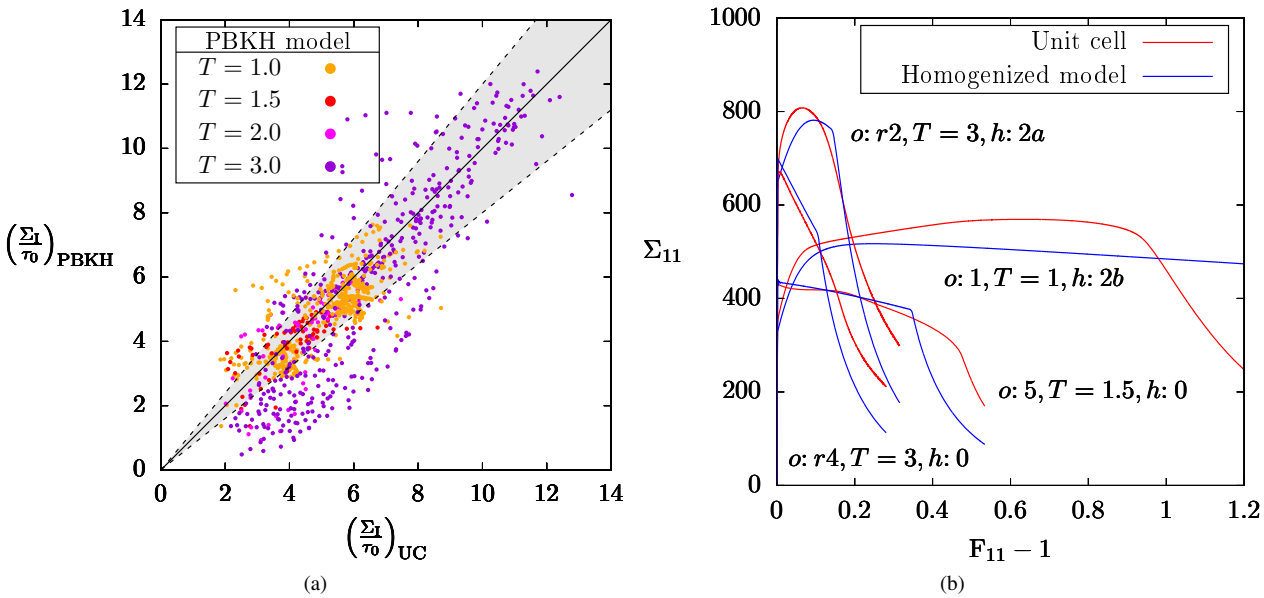
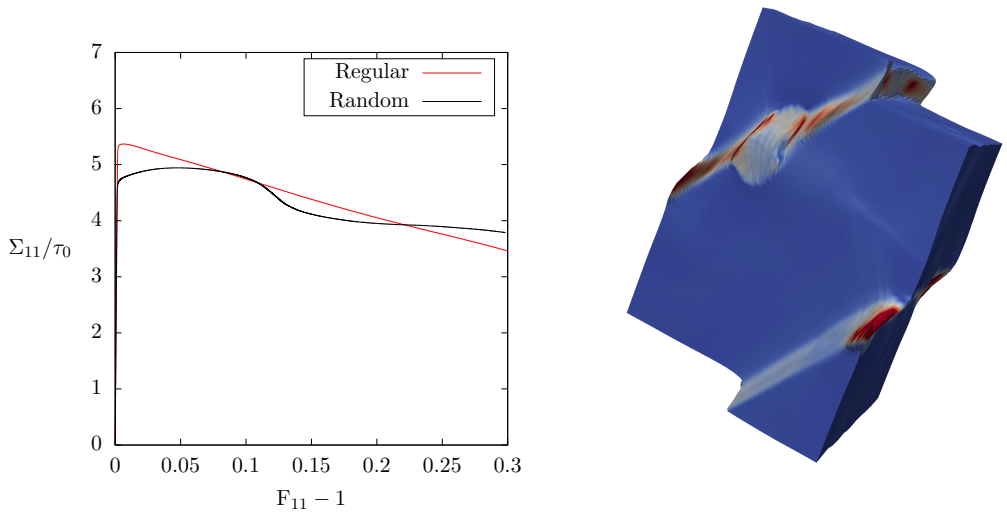


Figure 15: (a) Assessment of the homogenized model: normalized stress $\frac{\Sigma_{11}}{\tau_0}$ of both the unit-cell computation and the homogenized model considered are plotted against each other, each point corresponding to a sampled strain level in a given database simulation. Only unit-cell data corresponding to the absence of hardening or *2a* / *2b* PAN hardening are used; (b) Stress-strain curves of a representative set of simulations: various orientations (o), triaxialities (T) and hardening laws (h) are considered.

While a general perspective lies into the improvement of the models to better reproduce reference unit-cell results, an interesting improvement perspective is related to the distribution of voids. For both unit-cell simulations and the two homogenized models, an initially cubic array of voids have been considered. As shown for isotropic porous materials [71], void distribution affects both void growth and void coalescence modeling. In the former case, calibration of the parameters of the yield criteria is required. In the latter case, other deformation modes can be observed such as shear-assisted coalescence. As an example, the results of a simulation considering a random distribution of voids in a non-hardening single crystal is shown in Fig. 16 and compared to the case of a single void, for the same initial porosity, crystallographic orientation and mechanical loading condition. Slight differences are observed on the stress-strain curves (Fig. 16a), but the main difference lies in the coalescence deformation mode (Fig. 16b) where shear bands link adjacent voids. A shear-assisted coalescence yield criterion has been proposed for such situations [35] and its implementation is the next evolution step foreseen for the porous crystal models studied here. More importantly, finite strain porous single crystals unit-cell simulations considering random distributions of voids are definitely required to assess the occurrence of different coalescence modes (internal necking *vs.* shear-assisted). These simulations are numerically challenging, even for isotropic porous materials [72, 73], but appear as a milestone for the validation of homogenized models for porous single crystal plasticity.

Besides the perspectives of model improvement drawn previously, the main prospect is to use such models to perform ductile fracture simulations in single and poly-crystals, as done in [41, 36]. Different homogenized models should be studied in order to assess the effect of alternative modelling hypotheses on fracture strain / toughness and crack paths. Eventually, direct comparisons to experimental results – very limited in the literature – will be mandatory to validate the models.



(a) (b)

Figure 16: Finite strain porous ($f_0 = 1\%$) single crystal ($\phi_1 = 124.4°$, $\Phi = 34.2°$, $\phi_2 = 267.6°$) unit-cell simulations under axisymmetric loading conditions ($T = 1$) without hardening, for regular (cubic void distribution) and random (with 8 voids): (a) stress-strain curves and (b) typical local deformation gradient field in the coalescence regime in the random case for $F_{11} = 1.2$.

5. Conclusion

Homogenized constitutive equations for porous single crystals plasticity have been proposed in this study, accounting for both void growth and void coalescence deformation regimes. This set of equations is based on yield criteria available in the literature, and evolution laws are proposed to account for hardening and void shape. The homogenized model is designed to be as simple as possible from a numerical point of view by limiting the number of internal variables. This is reached by considering a single yield criterion for void growth regime, a single scalar value to describe hardening, a simplified finite strain framework and a numerical implementation coupling Newton-Raphson and fixed point algorithms. A database of finite strain porous unit-cell simulations has been gathered for FCC materials, including various hardening laws, crystallographic orientations, porosities and stress triaxiality ratios for axisymmetric loading conditions. The homogenized model predictions are found to be in good agreement with unit-cell simulations for low and medium hardening, whereas discrepancies are observed for strong hardening. The fact that deviations from unit-cell computations are of the same magnitude as the ones of an homogenized model with a more physical modelling of the growth phase [36] indicates that most of the features of porous single crystals plasticity are kept in the model proposed in this study. However, the model [36] underlines the importance of particular features such as structural hardening induced by lattice rotation. As a conclusion, the model proposed in this study can be used effectively to describe porous single crystals accurately in situations where rotation can be neglected, from low to medium hardening, with a limited number of internal variables and thus potentially as numerically efficient as homogenized models used for porous isotropic materials.

Acknowledgements

The authors thank Jacques Besson and Samuel Forest from Centre des Matériaux of Mines ParisTech for fruitful discussions.

CRediT authorship contribution statement

Cédric Sénac: Conceptualization, Methodology, Software, Investigation, Data curation, Writing - original draft, Writing - review & editing, Visualization. **Jean-Michel Scherer:** Conceptualization, Software, Investigation, Data curation, Writing - original draft, Writing - review & editing. **Jérémy Hure:** Conceptualization, Methodology, Software, Investigation, Data curation, Writing - original draft, Writing - review & editing, Funding acquisition. **Thomas Helfer:** Software. **Benoît Tanguy:** Conceptualization, Writing - review & editing, Funding acquisition.

Appendix A. Finite strain framework

The constitutive equations described in Section 3.1 for small strain theory are extended to finite strain theory using the logarithmic framework described in [62]. The advantage is this framework is to rely on pre- and post-processors to the small strain numerical implementation of the constitutive equations. The pre-processor is based on the definition of Hencky total strain as:

$$\underset{\sim}{\boldsymbol{\varepsilon}} = \frac{1}{2}\log\left(\underset{\sim}{\boldsymbol{F}}^T\underset{\sim}{\boldsymbol{F}}\right) \tag{A.1}$$

where $\underset{\sim}{\boldsymbol{F}}$ is the deformation gradient. Hencky strain tensor $\underset{\sim}{\boldsymbol{\varepsilon}}$ is used as the input for the integration of constitutive equations. The stress tensor computed $\underset{\sim}{\boldsymbol{T}}$ is not the Cauchy stress tensor $\underset{\sim}{\boldsymbol{\sigma}}$ required by the finite element solver, but the latter is found assuming duality: $\underset{\sim}{\boldsymbol{T}} : \dot{\underset{\sim}{\boldsymbol{\varepsilon}}} = \underset{\sim}{\boldsymbol{\sigma}} : \underset{\sim}{\boldsymbol{D}}$, where $\underset{\sim}{\boldsymbol{D}}$ is the Eulerian strain increment $\underset{\sim}{\boldsymbol{D}} = \dot{\underset{\sim}{\boldsymbol{F}}}\underset{\sim}{\boldsymbol{F}}^{-1}$ [74]. This framework thus allows to extend the applicability of small strain constitutive equations to finite strain, ensuring objectivity, and is available in the code generator `MFront` used in this study [75]. This framework has been shown to lead to good agreement for anisotropic plasticity to reference simulations using the multiplicative decomposition of the deformation gradient $\underset{\sim}{\boldsymbol{F}} = \underset{\sim}{\boldsymbol{F}}_\mathrm{e}\underset{\sim}{\boldsymbol{F}}_\mathrm{p}$ [62]. However, using the logarithmic framework for crystal plasticity, as done in this study in the limit $f \to 0$ for the growth yield criterion, has obvious limitations that are assessed here. Single slip, *e.g.*, $\underset{\sim}{\boldsymbol{F}} = \underset{\sim}{\mathbf{1}} + \gamma\,\underline{m}\otimes\underline{n}$ with associated eulerian strain increment $\underset{\sim}{\boldsymbol{D}} = \dot{\gamma}\,\underline{m}\otimes\underline{n}$ cannot be captured by Eq. A.1, being symmetric, leading to $\dot{\underset{\sim}{\boldsymbol{\varepsilon}}} = \frac{\gamma}{2}(\underline{m}\otimes\underline{n} + \underline{n}\otimes\underline{m})$. This is confirmed in Fig. A.17a where numerical simulations of simple shear with single slip are performed using multiplicative and logarithmic frameworks, without and with hardening. Similar discrepancy is observed for tensile loading on a crystal direction where single slip is involved in Fig. A.17b, where the logarithmic framework fails to recover the correct behavior.

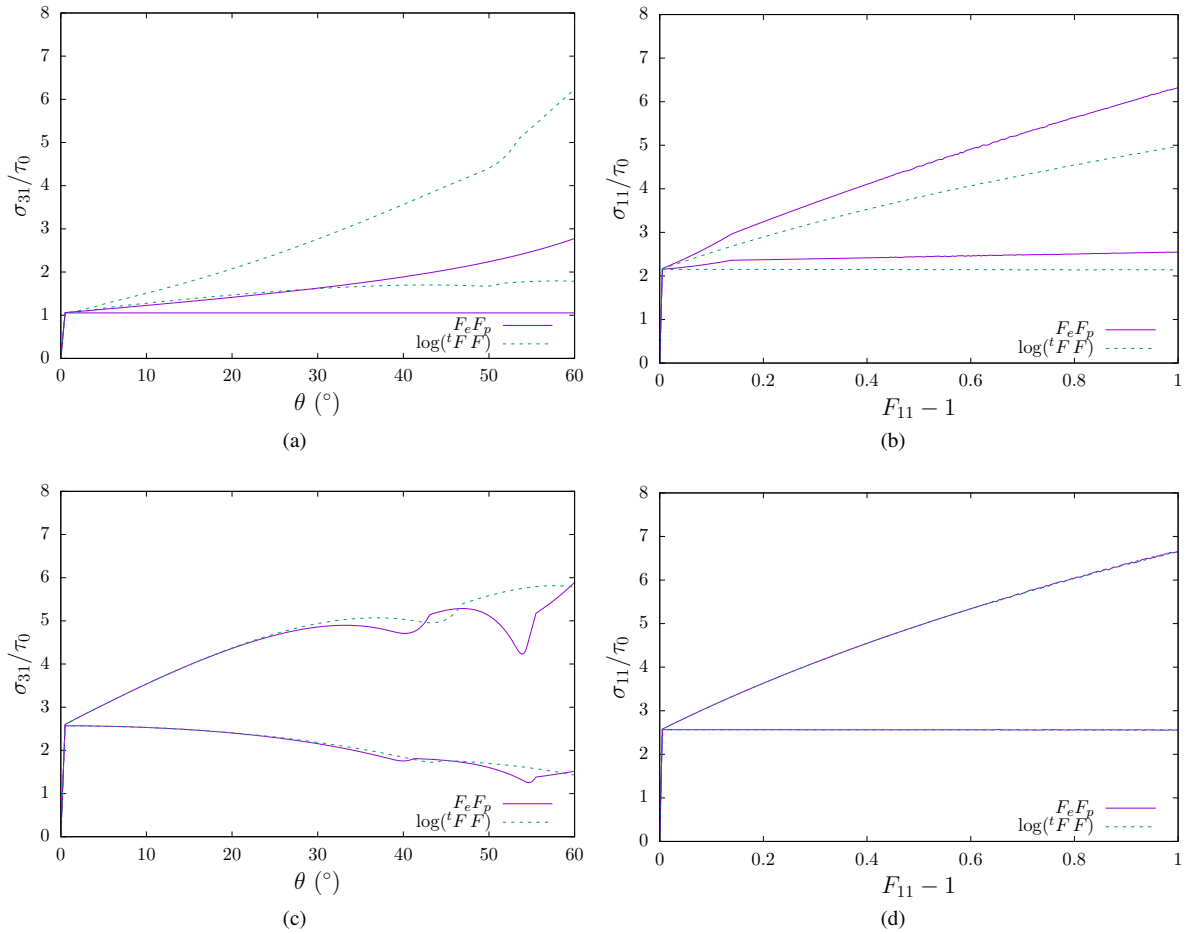


Figure A.17: Comparisons between finite strain crystal plasticity implementations based on the multiplicative decomposition of the deformation gradient ($\underset{\sim}{\boldsymbol{F}}_\mathrm{e}\underset{\sim}{\boldsymbol{F}}_\mathrm{p}$) and on the logarithmic framework: (a,c) simple shear: $\underset{\sim}{\boldsymbol{F}} = F_{31}\underline{e}_3\otimes\underline{e}_1$ (with $\theta = \operatorname{atan} F_{31}$); (b,d) uniaxial tensile: $\underset{\sim}{\boldsymbol{\sigma}} = \sigma\underline{e}_1\otimes\underline{e}_1$. 12 FCC slip systems are considered, and two sets of curves are plotted in each figure corresponding to different values of the Taylor hardening slope $H \in \{0, 100\}$ ($\tau_\mathrm{c} = \tau_0 + H\sum|\gamma_i|$). The crystal orientations along the 1-axis are (a) [1 1 1] (b) [$\bar{1}$ 2 5] (c, d) [1 0 0].

However, for symmetric orientations (Fig. A.17c,d), the logarithmic framework follows closely the results obtained with the multiplicative framework up to high strain levels. For simple shear (Fig. A.17c), deviations appear for shear angle higher than 60°. For tensile loading (Fig. A.17d), a perfect agreement is observed between the two frameworks. Therefore, the constitutive equations proposed in this study extended to finite strains using the logarithmic framework should be restricted in principle to symmetric orientations or high porosity / high mean stress levels where isotropic volumetric strain dominates. This corresponds in practice to high stress triaxiality or high porosity, which is the main focus of this study.

Appendix B. Yield criteria flow direction

Numerical implementation of the constitutive equations in the `MFront` code generator requires analytical expressions of yield criteria flow directions and their partial derivatives with respect to $\underset{\sim}{\Sigma}$. They are provided below.

Appendix B.1. Growth yield criterion

When dealing with yield criteria defined by $S(\sigma^*, \underset{\sim}{\Sigma}) = 0$, the two following equations are used:

$$\delta S = \frac{\partial S}{\partial \underset{\sim}{\Sigma}} : \delta\underset{\sim}{\Sigma} + \frac{\partial S}{\partial \sigma^*}\delta\sigma^* = 0 \tag{B.1}$$

$$\frac{\partial^2\sigma^*}{\partial\underset{\sim}{\Sigma}^2} = -\left(\frac{1}{\frac{\partial S}{\partial\sigma^*}}\right)\frac{\partial}{\partial\underset{\sim}{\Sigma}}\left[\frac{\partial S}{\partial\underset{\sim}{\Sigma}}(\cdot,\sigma^*(\cdot),...)\right] - \frac{\partial S}{\partial\underset{\sim}{\Sigma}}\otimes\frac{\partial}{\partial\underset{\sim}{\Sigma}}\left[\frac{1}{\frac{\partial S}{\partial\sigma^*}(\cdot,\sigma^*(\cdot),...)}\right] \tag{B.2}$$

Useful notations

$$S_{\mathrm{g}}^{(0)} \equiv \sum_{k=1}^{N}\left|\underset{\sim}{\boldsymbol{\mu}}_k^{(\mathrm{s})} : \underset{\sim}{\Sigma}\right|^n \tag{B.3}$$

$$\underset{\sim}{\boldsymbol{S}}_{\mathrm{g}}^{(\mathbf{1})} \equiv \sum_{k=1}^{N}\operatorname{sgn}\left(\underset{\sim}{\boldsymbol{\mu}}_k^{(\mathrm{s})} : \underset{\sim}{\Sigma}\right)\left|\underset{\sim}{\boldsymbol{\mu}}_k^{(\mathrm{s})} : \underset{\sim}{\Sigma}\right|^{n-1}\underset{\sim}{\boldsymbol{\mu}}_k^{(\mathrm{s})} \tag{B.4}$$

$$\underset{\approx}{\boldsymbol{S}}_{\mathrm{g}}^{(\mathbf{2})} \equiv \sum_{k=1}^{N}\left|\underset{\sim}{\boldsymbol{\mu}}_k^{(\mathrm{s})} : \underset{\sim}{\Sigma}\right|^{n-2}\underset{\sim}{\boldsymbol{\mu}}_k^{(\mathrm{s})}\otimes\underset{\sim}{\boldsymbol{\mu}}_k^{(\mathrm{s})} \tag{B.5}$$

Flow direction

$$\frac{\partial S_{\mathrm{g}}}{\partial\underset{\sim}{\Sigma}} = \frac{2}{\sigma_{\mathrm{g}}^*}\left[\frac{1}{\sigma_{\mathrm{g}}^*}\left(S_{\mathrm{g}}^{(0)}\right)^{\frac{2}{n}-1}\underset{\sim}{\boldsymbol{S}}_{\mathrm{g}}^{(\mathbf{1})} + \frac{1}{3}qf\kappa\sinh\left(\kappa\frac{\Sigma_{\mathrm{m}}}{\sigma_{\mathrm{g}}^*}\right)\underset{\sim}{\boldsymbol{I}}\right] \tag{B.6}$$

$$\frac{\partial S_{\mathrm{g}}}{\partial\sigma_{\mathrm{g}}^*} = -\frac{2}{(\sigma_{\mathrm{g}}^*)^2}\left[\frac{1}{\sigma_{\mathrm{g}}^*}\left(S_{\mathrm{g}}^{(0)}\right)^{\frac{2}{n}} + qf\kappa\sinh\left(\kappa\frac{\Sigma_{\mathrm{m}}}{\sigma_{\mathrm{g}}^*}\right)\Sigma_{\mathrm{m}}\right] \tag{B.7}$$

$$\underset{\sim}{\boldsymbol{n}}_{\mathrm{g}} = \frac{\partial\sigma_{\mathrm{g}}^*}{\partial\underset{\sim}{\Sigma}} = -\left(\frac{1}{\frac{\partial S_{\mathrm{g}}}{\partial\sigma_{\mathrm{g}}^*}}\right)\frac{\partial S_{\mathrm{g}}}{\partial\underset{\sim}{\Sigma}} \tag{B.8}$$

Flow direction first-order derivative

$$\frac{\partial^2 S_{\mathrm{g}}}{\partial\underset{\sim}{\Sigma}^2} = \frac{2}{\left(\sigma_{\mathrm{g}}^*\right)^2}\left[\left(S_{\mathrm{g}}^{(0)}\right)^{\frac{2}{n}-2}\left((n-1)S_{\mathrm{g}}^{(0)}\underset{\approx}{\boldsymbol{S}}_{\mathrm{g}}^{(\mathbf{2})} - (n-2)\underset{\sim}{\boldsymbol{S}}_{\mathrm{g}}^{(\mathbf{1})}\otimes\underset{\sim}{\boldsymbol{S}}_{\mathrm{g}}^{(\mathbf{1})}\right) + \frac{1}{9}qf\kappa^2\cosh\left(\kappa\frac{\Sigma_{\mathrm{m}}}{\sigma_{\mathrm{g}}^*}\right)\underset{\sim}{\boldsymbol{I}}\otimes\underset{\sim}{\boldsymbol{I}}\right] \tag{B.9}$$

$$\frac{\partial^2 S_{\mathrm{g}}}{\partial\underset{\sim}{\Sigma}\partial\sigma_{\mathrm{g}}^*} = -\frac{2}{(\sigma_{\mathrm{g}}^*)^2}\left[\frac{2}{\sigma_{\mathrm{g}}^*}\left(S_{\mathrm{g}}^{(0)}\right)^{\frac{2}{n}-1}\underset{\sim}{\boldsymbol{S}}_{\mathrm{g}}^{(\mathbf{1})} + \frac{1}{3}qf\kappa\sinh\left(\kappa\frac{\Sigma_{\mathrm{m}}}{\sigma_{\mathrm{g}}^*}\right)\underset{\sim}{\boldsymbol{I}} + \frac{1}{3}\frac{qf\kappa^2}{\sigma_{\mathrm{g}}^*}\cosh\left(\kappa\frac{\Sigma_{\mathrm{m}}}{\sigma_{\mathrm{g}}^*}\right)\Sigma_{\mathrm{m}}\underset{\sim}{\boldsymbol{I}}\right] \tag{B.10}$$

$$\frac{\partial^2 S_{\mathrm{g}}}{(\partial\sigma_{\mathrm{g}}^*)^2} = \frac{2}{(\sigma_{\mathrm{g}}^*)^3}\left[\frac{3}{\sigma_{\mathrm{g}}^*}\left(S_{\mathrm{g}}^{(0)}\right)^{\frac{2}{n}} + 2qf\kappa\sinh\left(\kappa\frac{\Sigma_{\mathrm{m}}}{\sigma_{\mathrm{g}}^*}\right)\Sigma_{\mathrm{m}} + \frac{qf\kappa^2}{\sigma_{\mathrm{g}}^*}\cosh\left(\kappa\frac{\Sigma_{\mathrm{m}}}{\sigma_{\mathrm{g}}^*}\right)\Sigma_{\mathrm{m}}^2\right] \tag{B.11}$$

$$\frac{\partial\underset{\sim}{\boldsymbol{n}}_{\mathrm{g}}}{\partial\underset{\sim}{\Sigma}} = \frac{\partial^2\sigma_{\mathrm{g}}^*}{\partial\underset{\sim}{\Sigma}^2} = -\left(\frac{1}{\frac{\partial S_{\mathrm{g}}}{\partial\sigma_{\mathrm{g}}^*}}\right)\left[\frac{\partial^2 S_{\mathrm{g}}}{\partial\underset{\sim}{\Sigma}^2} + \frac{\partial^2 S_{\mathrm{g}}}{\partial\underset{\sim}{\Sigma}\partial\sigma_{\mathrm{g}}^*}\otimes\frac{\partial\sigma_{\mathrm{g}}^*}{\partial\underset{\sim}{\Sigma}}\right] + \left(\frac{1}{\frac{\partial S_{\mathrm{g}}}{\partial\sigma_{\mathrm{g}}^*}}\right)^2\left[\frac{\partial S_{\mathrm{g}}}{\partial\underset{\sim}{\Sigma}}\otimes\left(\frac{\partial^2 S_{\mathrm{g}}}{\partial\underset{\sim}{\Sigma}\partial\sigma_{\mathrm{g}}^*} + \frac{\partial^2 S_{\mathrm{g}}}{(\partial\sigma_{\mathrm{g}}^*)^2}\frac{\partial\sigma_{\mathrm{g}}^*}{\partial\underset{\sim}{\Sigma}}\right)\right] \tag{B.12}$$

Appendix B.2. Coalescence yield criterion

As detailed in Section 3.1, M_1 and M_2 vary according to the coalescence plan normal $\underline{n}_I$, but are kept fixed once coalescence sets in. $\underline{n}_I$, $\underline{n}_{II}$ and $\underline{n}_{III}$ are the eigenvectors associated with principal stresses $\Sigma_I \geq \Sigma_{II} \geq \Sigma_{III}$.

Flow direction

$$\underset{\sim}{\boldsymbol{n}}_{\mathrm{c}} = \frac{1}{C_{\mathrm{f}}}\frac{\partial\Sigma_I}{\partial\underset{\sim}{\Sigma}} = \frac{1}{C_{\mathrm{f}}}\underline{n}_I\otimes\underline{n}_I \tag{B.13}$$

Flow direction first-order derivative

$$\frac{\partial\underset{\sim}{\boldsymbol{n}}_{\mathrm{c}}}{\partial\underset{\sim}{\Sigma}} = \frac{1}{C_{\mathrm{f}}}\frac{\partial^2\Sigma_I}{\partial\underset{\sim}{\Sigma}^2} = \frac{1}{C_{\mathrm{f}}}\sum_{J\in\{II,III\}}\frac{1}{\Sigma_I-\Sigma_J}\left[\underline{n}_I\otimes\underline{n}_J\otimes\underline{n}_I\otimes\underline{n}_J + \underline{n}_J\otimes\underline{n}_I\otimes\underline{n}_J\otimes\underline{n}_I\right] \tag{B.14}$$

Appendix C. Summary of the two homogenized models

The values of numerical parameters of the two homogenized porous models mentioned in this article are given in Table C.2. Moreover, the main equations for both models are summarized in Table C.3.

Parameter	PBKH model	HLS model
n	100	$\diagdown$
α	$\diagdown$	6.456
κ	0.49	0.513
q	1.66	1.471
κ^c	$\diagdown$	1.047
q^c	$\diagdown$	1.384
q_χ	$0.912 - 0.039T$	0.624
β	2.88	$\diagdown$

Table C.2: Numerical values of parameters used in the homogenized models.

Model equation	PBKH model	HLS model
Growth		
Yield criterion	$\left(\frac{\left(\sum_{k=1}^{N}\left\lvert\underset{\sim}{\boldsymbol{\mu}}_k^{(\mathrm{s})} : \underset{\sim}{\boldsymbol{\Sigma}}\right\rvert^n\right)^{\frac{1}{n}}}{\sigma_{\mathrm{g}}^*}\right)^2 + 2qf\cosh\left(\kappa\frac{\Sigma_{\mathrm{m}}}{\sigma_{\mathrm{g}}^*}\right) - 1-(qf)^2 = 0$	$\forall s \in [\![1,N]\!],\ \left(\frac{\left\lvert\underset{\sim}{\boldsymbol{\mu}}_s : \underset{\sim}{\boldsymbol{\Sigma}}\right\rvert}{\tau_s^*}\right)^2 + \alpha\frac{2}{45}f\left(\frac{\Sigma_{\mathrm{eq}}^{\mathrm{vM}}}{\tau_s^*}\right)^2 + 2qf\cosh\left(\kappa\frac{\Sigma_{\mathrm{m}}}{\tau_s^*}\right) - 1-(qf)^2 = 0$
Flow direction	$\underset{\sim}{\boldsymbol{n}}_{\mathrm{g}} = \frac{\partial\sigma_{\mathrm{g}}^*}{\partial\underset{\sim}{\boldsymbol{\Sigma}}}$	$\forall s \in [\![1,N]\!],\ \underset{\sim}{\boldsymbol{n}}_{\mathrm{g},s} = \frac{\partial\tau_s^*}{\partial\underset{\sim}{\boldsymbol{\Sigma}}}$
Coalescence		
Yield criterion	$\frac{\Sigma_I}{\sigma_{\mathrm{c}}^*} - C_{\mathrm{f}} = 0$	
C_{f}	$\frac{b}{\sqrt{3}}\left(2 - \sqrt{1+3\chi^4} + \ln\frac{1+\sqrt{1+3\chi^4}}{3\chi^2}\right)M_1 + t(W,\chi)\left(\frac{\chi^3-3\chi+2}{3\sqrt{3}W\chi}\right)M_2$	$(1-\chi^2)\left(0.1\left(\frac{1-\chi}{\chi W}\right)^2 + 1.2\sqrt{\frac{1}{\chi}}\right)$
Flow direction	$\underset{\sim}{\boldsymbol{n}}_{\mathrm{c}} = \frac{1}{C_{\mathrm{f}}}\frac{\partial\Sigma_I}{\partial\underset{\sim}{\boldsymbol{\Sigma}}}$	
Evolution laws		
Flow rule	$\dot{\underset{\sim}{\boldsymbol{\varepsilon}}}^{\mathrm{p}} = \dot{p}_{\mathrm{g}}\underset{\sim}{\boldsymbol{n}}_{\mathrm{g}} + \dot{p}_{\mathrm{c}}\underset{\sim}{\boldsymbol{n}}_{\mathrm{c}}$ $\dot{p}_i = \left(\frac{(\sigma_i^* - \tau^*)_+}{K}\right)^m$	$\dot{\underset{\sim}{\boldsymbol{\varepsilon}}}^{\mathrm{p}} = \sum_{k=1}^{N}\dot{\gamma}_k\underset{\sim}{\boldsymbol{n}}_{\mathrm{g},k} + \dot{p}_{\mathrm{c}}\underset{\sim}{\boldsymbol{n}}_{\mathrm{c}}$ $\dot{\gamma}_s = \left(\frac{(\tau_s^* - \tau_{\mathrm{c}}^s)_+}{K}\right)^m,\ \dot{p}_{\mathrm{c}} = \left(\frac{(\sigma_{\mathrm{c}}^* - \tau^*)_+}{K}\right)^m$ $\left(\frac{\Sigma_{\mathrm{eq}}^{\mathrm{vM}}}{\tau^*}\right)^2 + 2q^{\mathrm{c}}f\cosh\left(\kappa^{\mathrm{c}}\frac{\Sigma_{\mathrm{m}}}{\tau^*}\right) - 1 - (q^{\mathrm{c}}f)^2 \equiv 0$
f	$\dot{f} = (1-f)\mathrm{tr}\left(\dot{\underset{\sim}{\boldsymbol{\varepsilon}}}^{\mathrm{p}}\right)$	
W	$\dot{W} = \begin{cases}\frac{1}{W}\lvert T-2\rvert\dot{\varepsilon}_I & \text{(growth, } T<2\text{)}\\ -W\lvert T-2\rvert\dot{\varepsilon}_I & \text{(growth, } T\geq 2\text{)}\\ \frac{9\lambda}{4\chi}\left[1-\frac{2}{\pi}\frac{1}{\chi^2}\right]\dot{\varepsilon}_{\mathrm{eq}}^{\mathrm{p}} & \text{(coalescence)}\end{cases}$	$\dot{W} = 0$
λ	$\left(\frac{(C_I)^2}{C_{II}C_{III}}\right)^{\frac{1}{4}}$	$\lambda_c^0\left(\frac{L_I}{L_I^0}\right)^{\frac{3}{2}}\sqrt{\frac{1-f}{1-f_0}}$
χ	$q_\chi\left(\frac{6}{\pi}\frac{f\lambda}{W}\right)^{\frac{1}{3}}$	
FBZ hardening		
	$\dot{\tilde{\Gamma}} = \begin{cases}\frac{1}{C}\frac{\underset{\sim}{\boldsymbol{\Sigma}} : \dot{\underset{\sim}{\boldsymbol{\varepsilon}}}^{\mathrm{p}}}{(1-f)\tau^*} & \text{(growth)}\\ \frac{1}{C}\frac{\underset{\sim}{\boldsymbol{\Sigma}} : \dot{\underset{\sim}{\boldsymbol{\varepsilon}}}^{\mathrm{p}}}{\left(\frac{1}{f_{\mathrm{b}}}-1\right)f\tau^*} & \text{(coalescence)}\end{cases}$ $\dot{r_{\mathrm{D}}} = \left(\frac{1}{K_0}\sqrt{N-1}\sqrt{r_{\mathrm{D}}} - G_0 r_{\mathrm{D}}\right)\frac{\dot{\tilde{\Gamma}}}{12}$ $\tau^* = \tau_0 + \mu\sqrt{\sum_{k=1}^{N}a_{1k}\sqrt{r_{\mathrm{D}}}}$	$\forall s \in [\![1,N]\!],$ $\dot{r}_{\mathrm{D}}^s = \left(\frac{1}{K_0}\sqrt{\sum_{k=1}^{N}(1-\delta_s^k)r_{\mathrm{D}}^k} - G_0 r_{\mathrm{D}}^s\right)\lvert\dot{\gamma}_s\rvert$ $\tau_{\mathrm{c}}^s = \tau_0 + \mu\sqrt{\sum_{k=1}^{N}a_{sk}r_{\mathrm{D}}^k}$

Table C.3: Summary of the main equations used in the homogenized models.

References

[1] P. Noell, J. Caroll, B. Boyce, The mechanisms of ductile fracture, Acta Materiala 161 (2018) 83–98.
[2] A. A. Benzerga, J.-B. Leblond, Ductile fracture by void growth to coalescence, Advances in Applied Mechanics 44 (2010) 169–305.
[3] J. Besson, Continuum models of ductile fracture: A review, International Journal of Damage Mechanics 19 (2010) 3–52.
[4] A. Benzerga, J.-B. Leblond, A. Needleman, V. Tvergaard, Ductile failure modeling, International Journal of Fracture 201 (2016) 29–80.
[5] A. Pineau, A. Benzerga, T. Pardoen, Failure of metals: Part I - Brittle and ductile fracture, Acta Materiala 107 (2016) 424–483.
[6] A. Gurson, Continuum theory of ductile rupture by void nucleation and growth: Part I - Yield criteria and flow rules for porous ductile media, Journal of Engineering Materials and Technology 99 (1977) 2–15.
[7] G. Rousselier, Three-dimensional constitutive equations of damage and fracture: Finite deformation constitutive relations including ductile fracture damage, Pergamon Press (1981) 331–355.
[8] P. Ponte Castañeda, The effective mechanical properties of nonlinear isotropic composites, Journal of the Mechanics and Physics of Solids 39 (1991) 45–71.
[9] V. Tvergaard, On localization in ductile materials containing spherical voids, International Journal of Fracture 18 (1980) 237–252.
[10] V. Tvergaard, A. Needleman, Analysis of the cup-cone fracture in a round tensile bar, Acta Metallurgica 52 (1984) 157–169.
[11] K. Danas, P. P. Castañeda, A finite-strain model for anisotropic viscoplastic porous media: Part I - Theory, European Journal of Mechanics-A/Solids 28 (2009) 387–401.
[12] L. Morin, J.-B. Leblond, D. Kondo, A Gurson-type criterion for plastically anisotropic solids containing arbitrary ellipsoidal voids, International Journal of Solids and Structures 77 (2015) 86–101.
[13] E. Maire, P. Withers, Quantitative X-ray tomography, International Materials Reviews 59 (2014) 1–43.
[14] W. J. Mills, Fracture toughness of type 304 and 316 stainless steels and their welds, International Materials Reviews 42 (2) (1997) 45–82.
[15] S. Thomesen, O. S. Hopperstad, O. R. Myhr, T. Børvik, Influence of stress state on plastic flow and ductile fracture of three 6000-series aluminium alloys, Materials Science and Engineering: A 783 (2020) 139295.
[16] M. G. Stout, W. W. Gerberich, Structure/property/continuum synthesis of ductile fracture in Inconel alloy 718, Metallurgical Transactions A 9 (5 1978).
[17] V. Neustroev, F. Garner, Severe embrittlement of neutron irradiated austenitic steels arising from high void swelling, Journal of Nuclear Materials 286-288 (2009) 157–160.
[18] J. Crépin, T. Bretheau, D. Caldemaison, Cavity growth and rupture of β-treated zirconium: A crystallographic model, Acta Materiala 12 (1996) 4927–4935.
[19] M. Ding, J. Du, L. Wan, S. Ogata, L. Tian, E. Ma, W. Han, J. Li, Z. Shan, Radiation-induced helium nanobubbles enhance ductility in submicron-sized single-crystalline copper, Nano letters 16 (2016) 4118–4124.
[20] P. Barrioz, J. Hure, B. Tanguy, Effect of dislocation channelling on void growth to coalescence in FCC crystals, Materials Science and Engineering: A 749 (2019) 255–270.
[21] Y. X. Gan, J. W. Kysar, T. L. Morse, Cylindrical void in a rigid-ideally plastic single crystal: Part II - Experiments and simulations, International Journal of Plasticity 22 (2006) 39–72.
[22] P. Biswas, R. Narasimhan, A. Kumar, Interaction between a notch and cylindrical voids in aluminum single crystals: Experimental observations and numerical simulations, Journal of the Mechanics and Physics of Solids 61 (4) (2013) 1027 – 1046.
[23] G. Potirniche, J. Hearndon, M. Horstemeyer, X. Ling, Lattice orientation effects on void growth and coalescence in FCC single crystals, International Journal of Plasticity 22 (2006) 921–942.
[24] S. Ha, K. Kim, Void growth and coalescence in fcc single crystals, International Journal of Mechanical Sciences 52 (2010) 863–873.
[25] S. Yerra, C. Tekoğlu, F. Scheyvaerts, L. Delannay, P. V. Houtte, T. Pardoen, Void growth and coalescence in single crystals, International Journal of Solids and Structures 47 (2010) 1016–1029.
[26] B. Selvarajou, S. Joshi, A. Benzerga, Void growth and coalescence in hexagonal close packed crystals, Journal of the Mechanics and Physics of Solids 125 (2019) 198–224.
[27] J. Paux, R. Brenner, D. Kondo, Plastic yield criterion and hardening of porous single crystals, International Journal of Solids and Structures 132-133 (2018) 80–95.
[28] X. Han, J. Besson, S. Forest, B. Tanguy, S. Bugat, A yield function for single crystals containing voids, International Journal of Solids and Structures 50 (2013) 2115–2131.
[29] A. Mbiakop, A. Constantinescu, K. Danas, An analytical model for porous single cristals with ellipsoidal voids, Journal of the Mechanics and Physics of Solids 84 (2015) 436–467.
[30] D. Song, P. Ponte-Castañeda, A finite-strain homogenization model for viscoplastic porous single crystals: Part I - Theory, Journal of the Mechanics and Physics of Solids 107 (2017) 560–579.
[31] L. Joëssel, P.-G. Vincent, M. Gărăjeu, M. I. Idiart, Viscoplasticity of voided cubic crystals under hydrostatic loading, International Journal of Solids and Structures 147 (2018) 156–165.
[32] P.-G. Vincent, H. Moulinec, L. Joëssel, M. I. Idiart, M. Gărăjeu, Porous polycrystal plasticity modeling of neutron-irradiated austenitic stainless steels, Journal of Nuclear Materials 542 (2020) 152463.
[33] J. Paux, L. Morin, R. Brenner, D. Kondo, An approximate yield criterion for porous single crystals, European Journal of Mechanics A/Solids 51 (2015) 1–10.
[34] P. F. Thomason, A three-dimensional model for ductile fracture by the growth and coalescence of microvoids, Acta Metallurgica 33 (1985) 1087–1095.
[35] J. Hure, A coalescence criterion for porous single crystals, Journal of the Mechanics and Physics of Solids 124 (2019) 505–525.
[36] J.-M. Scherer, J. Besson, S. Forest, J. Hure, B. Tanguy, A strain gradient plasticity model of porous single crystal ductile fracture, Journal of the Mechanics and Physics of Solids 156 (2021) 104606.
[37] C. Ling, J. Besson, S. Forest, B. Tanguy, F. Latourte, E. Bosso, An elastoviscoplastic model for porous single crystals at finite strains and its assessment based on unit cell simulations, International Journal of Plasticity 84 (2016) 58–87.
[38] D. Song, P. Ponte-Castañeda, A finite-strain homogenization model for viscoplastic porous single crystals: Part II - Applications, Journal of the Mechanics and Physics of Solids 107 (2017) 580–602.
[39] A. Siddiq, A porous crystal plasticity constitutive model for ductile deformation and failure in porous single crystals, International Journal of Damage Mechanics 28 (2) (2019) 233–248.
[40] B. H. Frodal, S. Thomesen, T. Børvik, O. S. Hopperstad, On the coupling of damage and single crystal plasticity for ductile polycrystalline materials, International Journal of Plasticity 142 (2021) 102996.
[41] M. Khadyko, B. H. Frodal, O. S. Hopperstad, Finite element simulation of ductile fracture in polycrystalline materials using a regularized porous crystal plasticity model, International Journal of Fracture 228 (2021) 15–31.
[42] F. Roters, P. Eisenlohr, L. Hantcherli, D. Tjahjanto, T. Bieler, D. Raabe, Overview of constitutive laws, kinematics, homogenization and multiscale methods in crystal plasticity finite-element modeling: Theory, experiments, applications, Acta Materiala 58 (4) (2010) 1152 – 1211.
[43] E. P. Busso, G. Cailletaud, On the selection of active slip systems in crystal plasticity, International Journal of Plasticity 21 (11) (2005) 2212–2231.
[44] S. Forest, M. Rubin, A rate-independent crystal plasticity model with a smooth elastic–plastic transition and no slip indeterminacy, European Journal of Mechanics - A/Solids 55 (2016) 278–288.
[45] P. Franciosi, M. Berveiller, A. Zaoui, Latent hardening in copper and aluminium single crystals, Acta Metallurgica 28 (3) (1980) 273–283.
[46] L. Kubin, B. Devincre, T. Hoc, Modeling dislocation storage rates and mean free paths in face-centered cubic crystals, Acta Materialia 56 (20) (2008) 6040–6049.

[47] P. Franciosi, A. Zaoui, Multislip in fcc crystals a theoretical approach compared with experimental data, Acta Metallurgica 30 (8) (1982) 1627–1637.
[48] J. Hure, S. El Shawish, L. Cizelj, B. Tanguy, Intergranular stress distributions in polycrystalline aggregates of irradiated stainless steel, Journal of Nuclear Materials 476 (2016) 231 – 242.
[49] D. Peirce, R. J. Asaro, A. Needleman, Material rate dependence and localized deformation in crystalline solids, Acta Metallurgica 31 (12) (1983) 1951–1976.
[50] X. Han, Modélisation de la fragilisation due au gonflement dans les aciers inoxydables austénitiques irradiés, Ph.D. thesis, Thèse CEA, Ecole nationale supérieure des mines de Paris soutenue le 16/03/2017 (2012).
[51] J. Besson, R. Foerch, Object-oriented programming applied to the finite element method: Part I - General concepts, Revue Européenne des Éléments Finis 7 (1998) 535–566.
[52] CEA, AMITEX_FFTP, www.maisondelasimulation.fr/projects/amitex/html/ (2020).
[53] M. Kabel, S. Fliegener, M. Schneider, Mixed boundary conditions for fft-based homogenization at finite strains, Computational Mechanics 57 (2016) 193–210.
[54] C. Sénac, J.-M. Scherer, J. Hure, Porous single crystal unit-cell simulation database for ductile fracture by void growth and coalescence (2021). doi:10.5281/zenodo.5347763.
[55] M. Torki, A. Benzerga, J.-B. Leblond, On void coalescence under combined tension and shear, Journal of Applied Mechanics 82 (2015) 071005.
[56] M. Arminjon, A regular form of the Schmid law. Application to the ambiguity problem, Textures and Microstructures 14-18 (1991) 1121–1128.
[57] V. Gambin, Crystal plasticity based on yield surfaces with rounded-off corners, Zeitschrift für Angewandte Mathematik und Mechanik 71 (1991) 265–268.
[58] C. Sénac, J. Hure, T. Helfer, Homogenized material law for porous single crystal ductile fracture through void growth and coalescence (2021). doi:10.5281/zenodo.5575930.
[59] V. Vishwakarma, S. M. Keralavarma, Micromechanical modeling and simulation of the loading path dependence of ductile failure by void growth to coalescence, International Journal of Solids and Structures 166 (2019) 135 – 153.
[60] A. A. Benzerga, J.-B. Leblond, Ductile fracture by void growth to coalescence, Advances in Applied Mechanics 44 (2010) 169–305.
[61] C. Ling, J. Besson, S. Forest, B. Tanguy, F. Latourte, E. Bosso, An elastoviscoplastic model for porous single crystals at finite strains and its assessment based on unit cell simulations, International Journal of Plasticity 84 (2016) 58–87.
[62] C. Miehe, N. Apel, M. Lambrecht, Anisotropic additive plasticity in the logarithmic strainspace: Modular kinematic formulation and implementation based on incremental minimization principles for standard materials, Computer Methods in Applied Mechanics and Engineering 191 (2002) 5383–5425.
[63] A. A. Benzerga, J. Besson, R. Batisse, A. Pineau, Synergistic effects of plastic anisotropy and void coalescence on fracture mode in plane strain, Modelling and Simulation in Materials Science and Engineering 10 (1) (2001) 73–102.
[64] K. Enakoutsa, J.-B. Leblond, Numerical implementation and assessment of the glpd micromorphic model of ductile rupture, European Journal of Mechanics - A/Solids 28 (3) (2009) 445–460.
[65] L. Morin, D. Kondo, J. Leblond, Numerical assessment, implementation and application of an extended Gurson model accounting for void size effects, Eur. J. Mech. A/Solids 51 (2015) 183–192.
[66] T. Helfer, Assisted computation of the consistent tangent operator of behaviours integrated using an implicit scheme: Theory and implementation in `Mfront`, Tech. rep., CEA (2020).
[67] T. Helfer, B. Michel, J. Proix, M. Salvo, J. Sercombe, M. Casella, Introducing the open-source `MFront` code generator: Application to mechanical behaviours and material knowledge management within the pleiades fuel element modelling platform, Computers & Mathematics with Applications 70 (2015) 994–1023.
[68] J.-M. Scherer, J. Hure, A size-dependent ductile fracture model: Constitutive equations, numerical implementation and validation, European Journal of Mechanics - A/Solids 76 (2019) 135–145.
[69] T. DebRoy, H. Wei, J. Zuback, T. Mukherjee, J. Elmer, J. Milewski, A. Beese, A. Wilson-Heid, A. De, W. Zhang, Additive manufacturing of metallic components – Process, structure and properties, Progress in Materials Science 92 (2018) 112–224.
[70] L. Morin, J.-C. Michel, J.-B. Leblond, A Gurson-type layer model for ductile porous solids with isotropic and kinematic hardening, International Journal of Solids and Structures 118-119 (2017) 167–178.
[71] F. Fritzen, S. Forest, T. Bohlke, D. Kondo, T. Kanit, Computational homogenization of elasto-plastic porous metals, International Journal of Plasticity 29 (2012) 102–119.
[72] J. Hure, Yield criterion and finite strain behavior of random porous isotropic materials, European Journal of Mechanics - A/Solids 85 (2021) 104143.
[73] C. Cadet, J. Besson, S. Flouriot, S. Forest, P. Kerfriden, V. de Rancourt, Ductile fracture of materials with randomly distributed voids, International Journal of Fracture 230 (2021) 193 – 223.
[74] M. Abbas, Model of great deformations `GDEF_LOG`, Tech. rep., EDF / Code_Aster (2016).
[75] T. Helfer, C. Ling, Écriture de lois de comportement mécaniques en grandes transformations avec le générateur de codes `MFront`, Tech. rep., CEA (2014).